Spring 6-14-2024

Modeling exciton delocalization and transport in PDBD-T-2F with the line-dipole improvement for coupling calculation

Brian Dvorak
DePaul University, bdvorak@depaul.edu

Modeling exciton delocalization and transport in PDBD-T-2F with the line-dipole improvement for coupling calculation

Brian Dvorak

Table of Contents

Abstract

A non-atomistic representation of the conjugated polymer PDBD-T-2F was constructed to model exciton delocalization and transport in the material. A Hamiltonian was built in the site basis to model the energy transfer, using excitation energies calculated using density functional theory and inter-site through-space coupling values calculated with either density functional theory or the newly integrated line-dipole approximation. The Hamiltonian allowed calculation of the excitation energies available for each system, prediction of the absorption spectrum, and simulation of the dynamics of exciton transport. For realistic crystal sizes at room temperature, the model predicts a band gap at 1.9 eV with decreasing absorption toward higher energies. This aligns with the absorption peaks in the experimental spectrum for PDBD-T-2F solvated in 1,2-dichlorobenzene as reported by Kroh *et al.* Exciton propagation through time illustrated the expected anisotropic, J-aggregate behavior. Delocalization in the pi-stacking direction was greater than the delocalization along either the intra-lamellar or the down-chain directions of the model. As a logistic benefit, the low-computation cost of this model enables at-will comparison between experimental results and simulated coupling behavior for closely packed systems with extended conjugation.

Section 1: Introduction & Background

Simulation of electronic dynamics is an invaluable asset in the characterization of molecular electronic technologies such as solar cells. While the pertinent timescales for these mechanisms can be studied by precise instrumentation, computational modeling offers flexibility to theoretically test diverse system parameters.[1] Experimental data often captures the net result of a system, which may have multiple competing pathways. In contrast, a computational analysis method allows manipulation of each component to characterize, and weight the significance of, each competing pathways' interactions.

Computational modeling compliments experimental data. Modeled systems input known molecular properties and output the resultant macroscopic behavior. Matching computational results with experimental observations can indicate which microscopic conditions are probable key factors in an experiment.[2] Models are only suitable when they satisfy two conditions. First, the computation time to generate an appropriate dataset must be reasonable with the available computing resources. Second, the assumptions used to build the system must be justified based on theory, empirical behavior, benchmarked against other calculation methods. Conclusions must be analyzed in light of the assumptions used to build the model. Computational chemistry has been used to understand cellular processes including photosynthesis and respiration.[3] It has also been used to describe immeasurable, quantized phenomena such as a Rydberg array.[4] Accepting the computing constraints and the limitations assumptions bring, computer simulations are still an excellent method to generate and describe meaningful results.[5]

Developing organic photovoltaic cells [OPVs] with improved efficiency and physical properties is of great financial interest. These cells rely on exciton generation and transport through the medium, as outlined in Section 1.2. While most of today's commercially available photovoltaic cells use doped inorganic silicon to absorb the light energy, OPVs can be precisely tuned for the environment and performance needs of each application.[6] This flexibility in molecular design and manufacturing processes helps address many of the logistic disadvantages

of solar cells. Weight, surface reflectance, and dust adhesion can all be lowered through structural modifications to develop customized OPV options, which maximize the efficiency in a specific application environment.[7] The absorption spectra of OPVs can be tuned to better match the solar spectrum to improve the OPV's efficiency.[8,9] Through changing the degree of conjugation, engineered polymers enable researchers to decouple the absorption spectrum of the material from its charge generation properties, which is a tremendous benefit. In comparison, inorganic materials which have fixed bulk absorption and charge generation properties which limit their cell designs. OPVs also offer increased physical flexibility. Nonetheless, there are unsolved challenges for OPVs including, but not limited to power conversion efficiency and long term environmental durability.

Power conversion efficiency is the percentage of incident light energy that is converted to electricity, and it is a useful metric as it directly compares how well systems convert electronic states to usable current. This metric looks past differences in absorption so a system with increased absorption is not considered more efficient if it has the same conversion rate.[10] In research this absorption-independent metric is useful as the lab system processing methods for different materials may be at different stages within the optimization. It is valuable to recognize the systems that have high power conversion efficiency even if absorption at certain wavelengths is low.

1.1 PDBD-T-2F polymer system

The conjugated polymer poly[[4,8-bis[5-(2-ethylhexyl)-4-fluoro-2-thienyl]benzo [1,2-b:4,5-b′]dithiophene-2,6-diyl]-2,5-thiophenediyl[5,7-bis(2-ethylhexyl)-4,8-dioxo-4H,8H-be nzo[1,2-c:4,5-c′]dithiophene-1,3-diyl]-2,5-thiophenediyl] is often named PDBD-T-2F or PM6 in published literature (Figure 1a).

The alternating regimes of the PDBD-T-2F repeating unit have a push-pull design.[20] The benzodithiophene moiety of PDBD-T-2F donates electron density while the

benzodithiophene-dione moiety is electron deficient.[22] Together these components produce a useful band gap in the visible region.[23] PDBD-T-2F is used as an electron donor in OPV devices, often coupled with the organic small molecule Y6 as an electron acceptor (Figure 1b).[11-14] The two component system has reached power conversion efficiencies of 18% in lab bulk heterojunction designs.[15] For comparison, crystalline silicon reached an experimental power conversion efficiency of 26% in 2018.[16] Based on the absorption band gap and the Shockley-Queisser limit, the maximum power conversion efficiency is 33% for silicon single junction systems, 17% for standalone PDBD-T-2F, or 32% for standalone Y6.[17] As a bulk heterojunction, a PDBD-T-2F:Y6 blend could in theory outperform the Shockley-Queisser limit as PDBD-T-2F can convert more of the higher energy photons to electricity, while the Y6 is still excited by lower energy photons that cannot excite PDBD-T-2F.

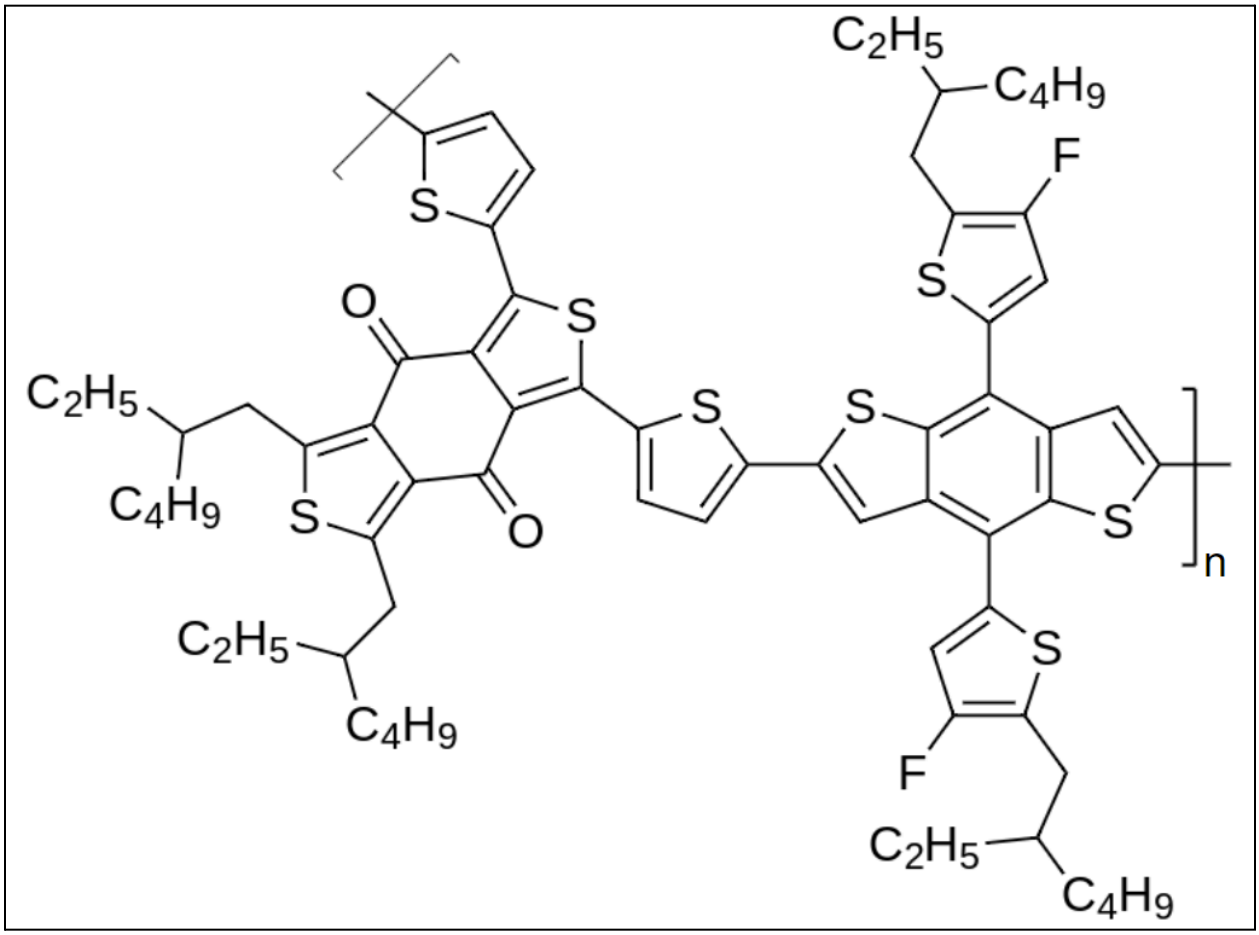

Figure 1a *The PDBD-T-2F repeating unit chemical structure.*

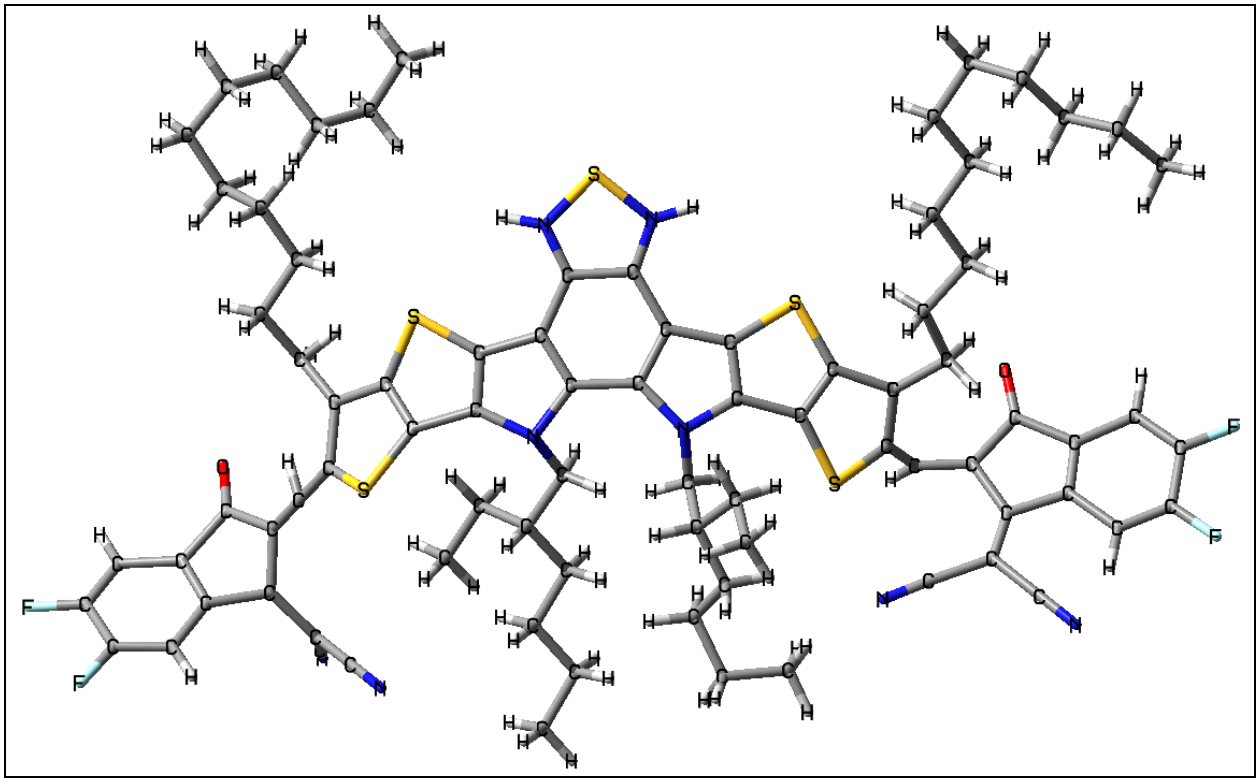

Figure 1b *Y6 electron acceptor chemical structure.*

In designing an OPV system, combining PDBD-T-2F with Y6 is attractive as the molecules have complementary absorption spectra so together they can utilize a higher fraction of the solar irradiance compared to other historic designs such as PDBD-T-2F:fullerene.[18,19] PDBD-T-2F and fullerene both have peak absorption in the blue-green wavelengths, which means they inhibit each other's absorption.[21]

Characterizing how excitons, defined below, travel through PDBD-T-2F provides insight into how PDBD-T-2F:Y6 systems should be blended to create the most efficient domain sizes. A system with non-optimal domains may generate excitons which recombine or are trapped before charge separation.

Despite silicon solar cells' headstart in development for the consumer market, OPVs have several advantages over the inorganic options that warrant the continued study of organic photovoltaic generation mechanisms. While there are a limited number of inorganic crystals with

suitable band gaps excited by solar radiation, organic polymeric materials' band gaps can be tuned over a larger range to best absorb sunlight.[25,26]

Energy band gaps are adjusted by changing the electron density and available orbitals within the molecule. Larger adjustments are made by changes in the bonding structure, which affect conjugation. Extending conjugation networks decreases the HOMO-LUMO gap when all else is held constant. This redshifts the band gap because less energetic, longer wavelength photons can now excite an electron to the higher energy state. Smaller adjustments are made by changing the electronegativity of atoms in the molecule or by adding functional groups with donate or withdraw electron density. In PDBD-T-2F, both electron withdrawing fluorine substituents on the thiophene rings decrease the band gap and redshift the absorptions spectrum.

Increasing conjugation is a practical method for organic systems to lower the band gap energy into the visible range in the solar spectrum, which explains why conjugated polymers are popular materials in the photovoltaic field. While UV radiation can access the larger band gaps of systems with shorter conjugation, the total energy of solar UV light (<380 nm) is much less than the solar visible light (380-780 nm) which is slightly more than the energy in solar IR light (>780 nm) (Figure 2). In addition, increasing the absorption of these higher energy UV photons can accelerate premature polymer degradation. By varying the repeating unit chemistry, the number average chain length, the polydispersity, or the crystallinity fraction, the exciton delocalization behavior once excited can also change. These modifications also change the physical properties of the organic material so it is possible to make stronger or more ductile systems compared to traditional inorganic designs.[27]

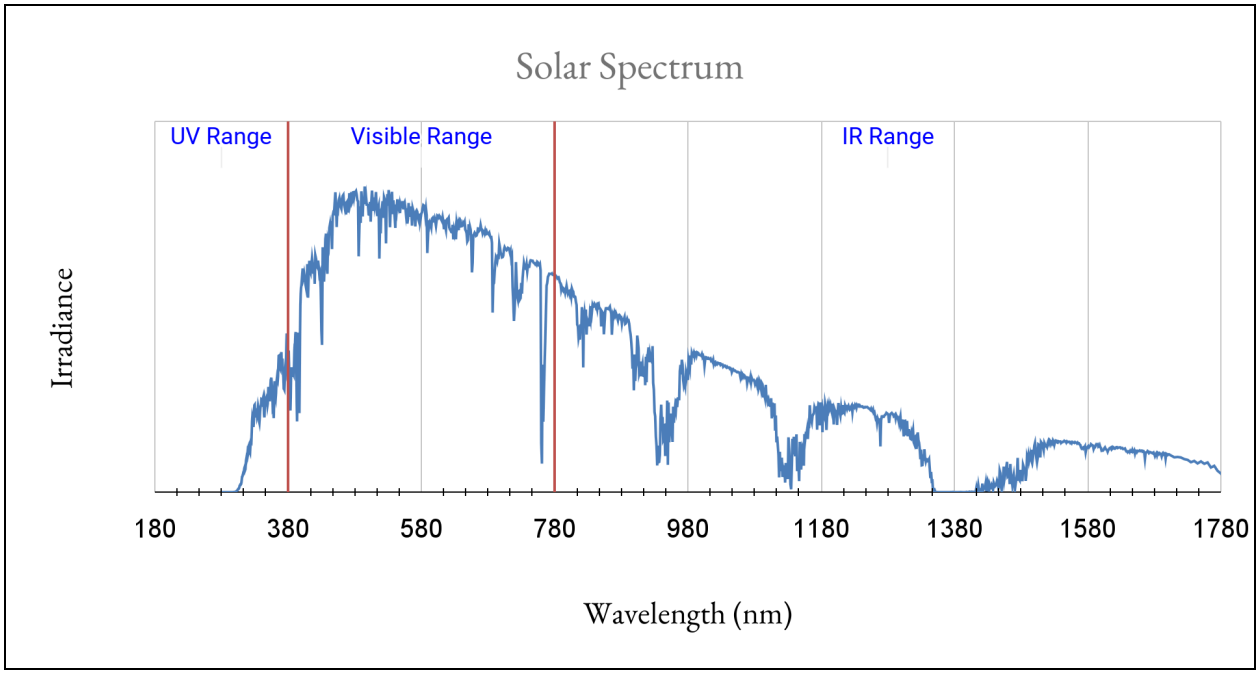

Figure 2 *Terrestrial solar irradiance spectrum. Spectrum generated from NREL SMARTS 2.9.2 model using ASTM G-173 conditions which average seasonal and geographic variation.*[28,29]

1.2 Exciton behavior in OPVs

For both inorganic and organic cell designs, there are three fundamental steps to capture the solar energy: excitation generating an exciton, charge separation, and collection of the nascent charges for incorporation into an auxiliary electric circuit (Figure 3). The models used in this work simulate the generation and transport of the excitons on short femtosecond [fs] timescales where quantum effects are important.

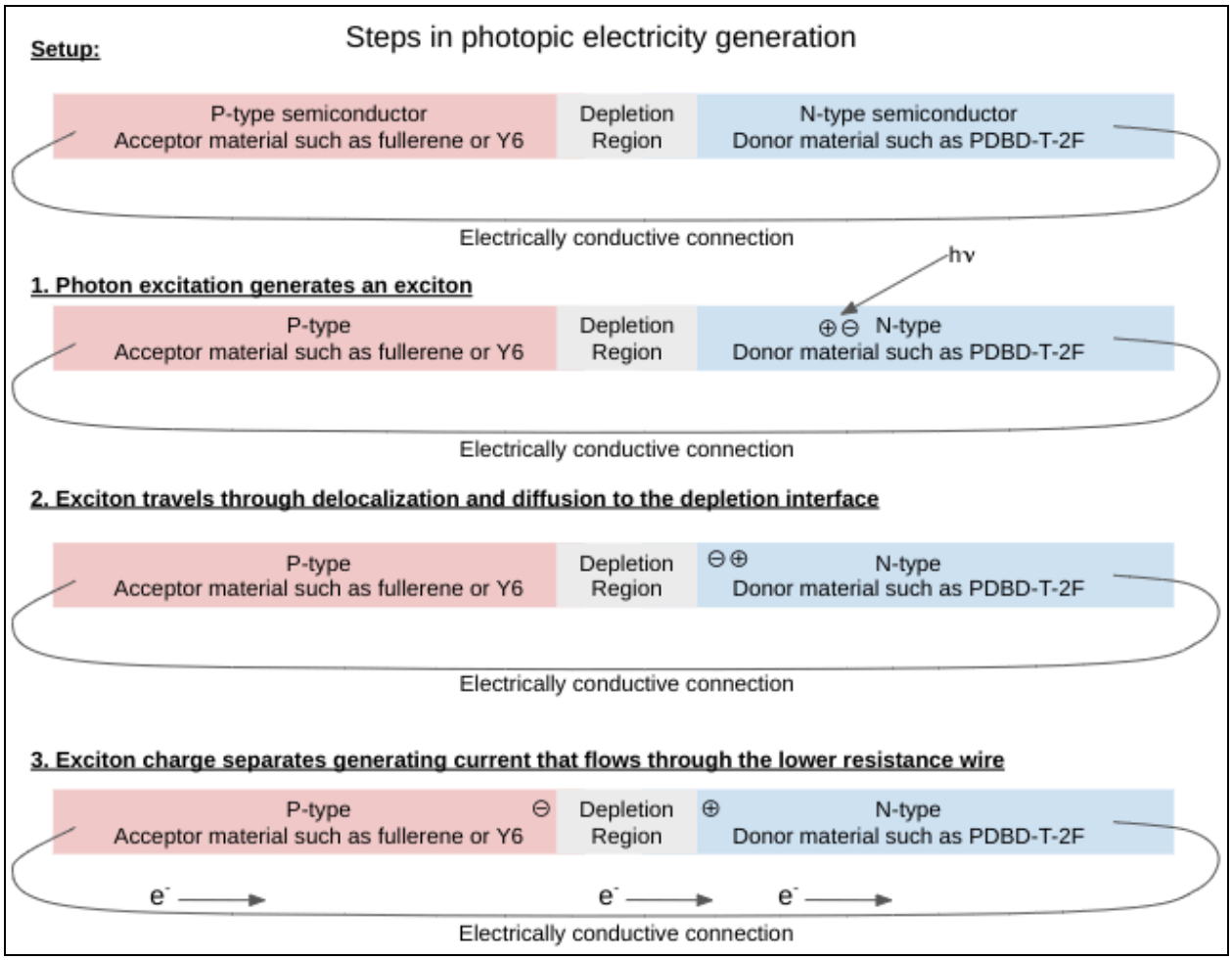

Figure 3 *P-type electron acceptor semiconductors and N-type electron donor semiconductors are paired in photovoltaic devices. At the p-n junction electrons travel to the acceptor creating a depletion zone with a standing electric field from the separated charge. A photon excites an electron to the conduction band forming an exciton. If this exciton separates the hole and electron across the junction, the electron can travel back to the positive N-type material through the low resistance wire yielding productive current. Bilayer devices have one pair of semiconductors as shown in this figure with a single interface located between the semiconductors for charge separation. Bulk heterojunction designs have many P and N domains intermixed with charge separation interfaces available on multiple sides of each domain.*

The exciton is created when a photon of appropriate energy irradiates a donor substrate, exciting an electron across the band gap. With only one remaining electron in the ground state orbital after excitation, the original ground state orbital acts as a comparatively positive area in the system's electron density due to the atom's unchanged protons. This pseudo particle is defined as a hole. Collectively, this hole and the excited electron are referred to as an exciton pair. They are coulombically attracted to each other, but this force can be overcome with appropriate system design. The typical distance between this electron and hole pair determines the class of exciton. The Frenkel model exciton keeps the hole and electron as immediate neighbors traveling as a bound pair through the medium. The Mott model allows further separation between the hole and electron, which physically occurs in higher dielectric materials. Nevertheless, these models are on a spectrum of possibilities and even the Frenkel description typically used for OPVs allows some separation between the hole and the electron.[30] The exciton must successfully migrate through the donor substrate to the interface with the electron acceptor material to initiate charge separation.[31]

Utilizing excitons is limited by their finite lifetime. In conjugated organic materials irradiated with light, the singlet excitation will rapidly decay to the ground vibrational level of the first excited state through non-radiative pathways, then only persist in this excited state for nanoseconds (Figure 4).[25,32] Mechanisms in which the exciton relaxes to the ground state, either radiatively or non-radiatively, are collectively called recombination. The exciton must reach the p-n junction prior to recombination or else the photon's energy is lost as heat.

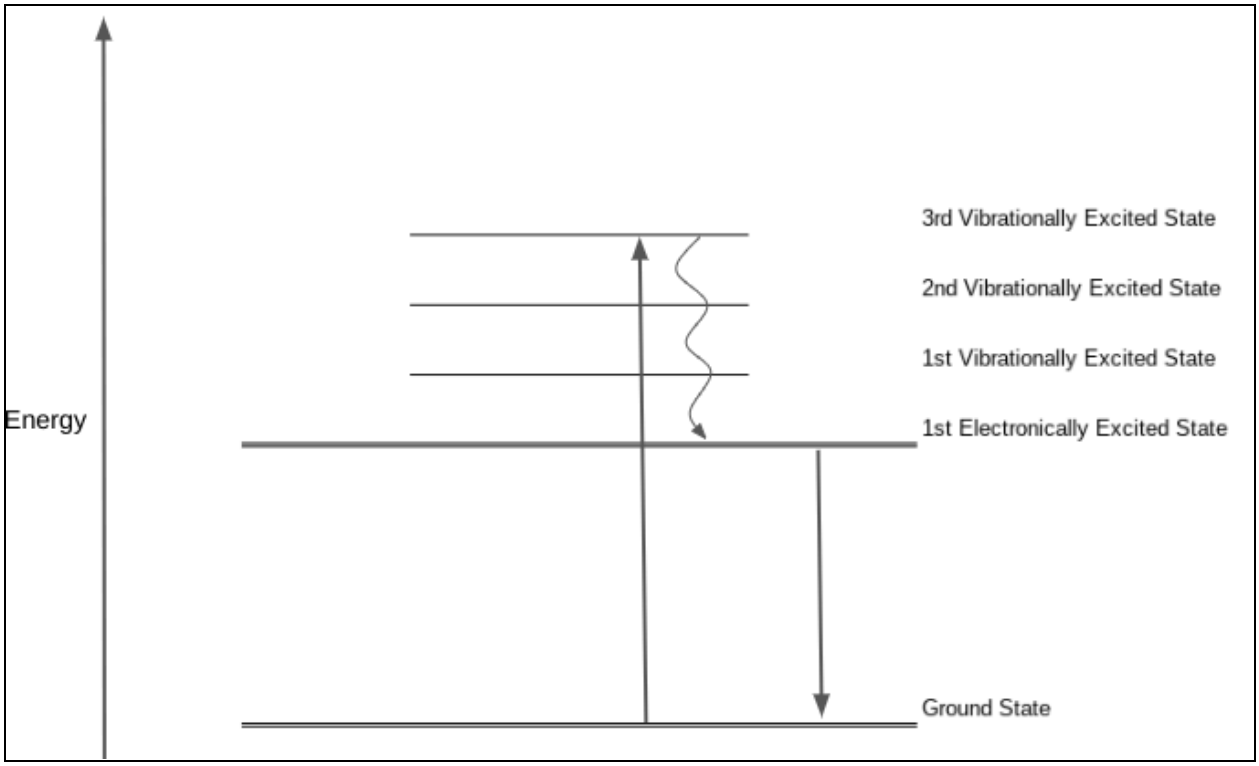

Figure 4 *Jablonski diagram illustrating electron excitation from the ground state, subsequent non-radiative transition to the ground vibrational excited state, and fluorescence back to the ground state.*

Exciton migration is the focus of this research as it is a critical step determining OPV efficiency. The charge separation is only possible at heterogeneous donor/acceptor material junctions in the matrix, so exciton migration to these points from the photon absorption point is necessary. It is challenging to empirically correlate the behavior of bulk heterojunction systems to a specific dimension of the domains. Physical processing techniques for particle homogenization, separation, milling, and agglomeration can impact the material behavior or alignment of the polymer aggregates, which makes it impossible to know all of the spatial interactions within a given physical sample.[33] This makes correlating the observable properties of devices with the microscopic properties of polymer aggregates challenging.

The microscopic control and detail available in computational modeling can help reveal the structure-function relationship that is critical to understand how excitons migrate. While

many OPVs are crystalline with uniform structure to the boundary, some are paracrystalline and add ambiguity to the polymer orientations within each domain.

An exciton's position is controlled by two different mechanisms: classical diffusion and quantum mechanical delocalization. Classical diffusion describes how an exciton pair moves within a domain at longer, near-nanosecond timescales. Faster quantum delocalization employs the wave-like properties of the exciton and describes how the exciton is distributed across multiple sites' combined orbitals at the same time.

Classical diffusion's movement is a function of the domain's dielectric constant. Organic polymers have lower relative dielectric constants only one third that of inorganic crystalline silicon.[25] Because of the lower diffusive movement, quantum delocalization may have a larger impact on organic exciton movement than it does for inorganic excitons, which makes new research into delocalization factors important.[9] Together with classical diffusion this superposition of the exciton affects how far an exciton can travel before recombination. In older OPV systems excitons typically travel 5-10 nm in conjugated polymers before recombinative quenching.[25] Newer OPV designs demonstrate exciton diffusion lengths up to 45 nm.[34] These longer diffusion lengths are critical to build practical systems in which the absorbed photons can travel across dozens of polymer strands to reach the junction of the domains maximizing efficiency.

1.3 Computational approach

The modeling in this project is centered around a site basis Hamiltonian operator that describes the energetics of a polymer aggregate using a basis set of singlet excitations of individual monomer units. These sites are non-atomic in nature, representing points in the model space used to calculate the relative geometric alignments without considering the molecular-scale nuances that would be present in a fully atomistic model. The Hamiltonian is consistent with the Born-Oppenheimer approximation and omits electron spin and vibronic effects, representing

excitation of individual sites to only the lowest singlet excited state in the vibrational ground state. Electronic coupling between the sites is calculated pairwise, as a through-space coupling. As the conjugation extends through the backbone of a polymeric PDBD-T-2F system, this model's simplification to set through bond coupling to zero is an impactful omission. Systems which include through bond coupling are expected to have increased interaction in the down-chain direction (parallel to the polymer backbone) compared to this model.

The Hamiltonian dictates how the excitons move through the system via electronic coupling between the sites. When there is coupling between sites, the off-diagonal values are non-zero and exciton population transfers through space to nearby sites over time. Diagonalizing a Hamiltonian that had non-zero off-diagonal values will produce an eigenmatrix. This eigenmatrix describes the photon energies that would absorb based on the system's Hamiltonian. These absorption energies are stationary in time because the Hamiltonian in this model is static during each simulation. These orthogonal absorption energy vectors define the exciton basis set and transform the system between the exciton basis and the site basis. Transforming the absorption energy matrix into the site basis lets the model show how the exciton is delocalized across the sites when a photon is absorbed at the specified energy.

Exciton mobility can be affected by a system's crystal size, crystal shape, coupling strength, intermonomer spacing, site excitation energy, as well as the variance across the system for any of these parameters. Modeled results are useful to design future generations of OPVs because they discern which parameters are most influential. Modeled crystal size may set the optimal polymer aggregate size or minimum percent crystallinity for a system before efficiency is lost. Crystal shape can shed light on which OPV processing methods are ideal or which intermonomer stacking dimensions are influential. Inter monomer spacing and repeating unit chemistry can impact the delocalization shape affecting which crystal face it is most efficient for stacking aggregate junctions. Site energy noise variance impacts the shape of each eigenstate. While a physical experiment may isolate some of these properties, many are tied together

constraining interpretation. Modeling can effectively narrow down the ideal conditions or explain the mechanisms that drive system performance to better direct which physical experiments are worthwhile.

1.4 Mechanisms of lost efficiency

Excitons are trapped when they do not travel close enough to the donor/acceptor material interface for charge separation before they are quenched. Trapping can be self-caused through quenching mechanisms within the local molecular structure.[35,36] Trapping can also be caused by low-energy defects within the lattice that prevent further travel. If the exciton recombines before it reaches and separates at an interface, then it does not generate useful charge carriers and the quantum efficiency decreases.

Lattice defect trapping may be more prevalent in organic systems compared to inorganic systems because of lower intermolecular forces that facilitate more molecular packing irregularities at the same system thermal energy.[37] These defects lower the efficiency of OPV devices and can be an inspiration for thinner laboratory experimental systems where it is easier to produce a homogeneous lattice.

An exciton pair can terminate through self-recombination on picosecond timescales if the attractive forces between the pair are greater than the dispersive forces acting on the pair. Excitons can also be non-productively quenched if parts of two separate pairs terminate through biexcitonic recombination. Because this second process requires two excitons to diffuse to a common location, this recombination process occurs on slower, nanosecond timescales.[25]

Anderson localization is one class of exciton trapping. Anderson localization occurs at high temperatures in disordered systems where the structural or chemical differences within the lattice inhibit diffusion due to diminished electronic overlap.[37] The effects of Anderson localization are more pronounced in lower order systems such as 2-dimensional thin films or 1-dimensional wires.

At larger system scales composed of many crystals, the thickness of the OPV has performance and economic implications. Thicker OPVs require more material to produce, increasing the cost. However, manufacturing constraints may limit the minimum thickness that can be commercially produced with acceptable uniformity. The thickness also affects the trapping behavior, absorption profile, and required exciton travel length to reach the interface. In bilayer systems that are too thick, efficiency drops because excitons only form at the front surface and cannot reach the back conductive surface for harvesting before the excited state non-radiatively recombines. Prospective OPV systems like PDBD-T-2F show similar efficiency in bulk heterojunction designs as they do in pseudo-planar heterojunctions, so it is valuable to consider each design's potential efficiency effects when interpreting experimental results.[43] Thicker bilayer systems are also affected by charge collection narrowing [CCN], where wavelengths with lower extinction coefficients exhibit increased relative efficiency because photons with this wavelength travel further into the system. This reduces the distance generated excitons must travel.[24] Wavelengths with high extinction coefficients interact with the system sooner in space, which forces the excitons to travel further through the system to reach the back surface acceptor (The photovoltaic in Figure 3 behaves differently if it is irradiated from the left, right, or topside as distance to the interface and the transport medium changes). Utilizing CCN, a system's absorption spectrum can be adjusted by varying the macroscopic thickness of the system without having to change crystal size or repeating chain chemistry.

Section 2: Methods

2.1 Building the Hamiltonian in the site basis

The Hamiltonian operator is a square matrix with rows and columns equal to the number of sites available for the exciton in the system (Equation 1). Each site in the model is designed to represent one monomer unit of PDBD-T-2F. The site basis Hamiltonian is defined by the lowest energy singlet excitations of monomer sites, $|m\rangle$, the singlet excitation energy, ε, the electronic

coupling between each pair of sites, J_{mn}, and a site energy noise parameter, σ. The coupling between sites is a function of the transition dipole for excitation of the monomer and the relative geometry of each pair of sites. In this model, the dipoles are all assumed to be parallel and aligned down the polymer chain backbone direction.

$$\widehat{H}_{electronic} = \sum_{m=1}^{N} [\varepsilon + \sigma]|m\rangle\langle m| + \sum_{m \neq n} J|m\rangle\langle n| \quad (1)$$

The excitation energy and transition dipole magnitude were calculated with density functional theory [DFT] for each monomer site (described in Section 2.2.2). DFT was also used to calculate the electronic coupling between closely spaced sites (Section 2.3.3). Electronic couplings between further separated pairs were calculated with the computationally efficient line dipole method (Section 2.3.2).

In this model, electronic coupling was calculated with only Coulombic interactions between the transition densities of the two sites as inputs. Dexter exchange coupling, which is an interaction effect between nearby orbitals, was omitted, which may lead to underestimation of coupling for very closely spaced sites where the exchange coupling effect is largest.[38]

2.2 Determination of PDBD-T-2F site properties

Several material properties specific to the PDBD-T-2F must be used to build the Hamiltonian for this model. These properties were either gathered from reported Grazing Incident X-ray Scattering [GIXS] results for PDBD-T-2F (Section 2.2.1) or preset with DFT calculations (Section 2.2.2). DFT calculations were used to set the monomer site excitation energy, ε, the total transition dipole vector magnitude for the monomer's first singlet excited state, $|\hat{u}|$, and the coupling values for the nearest neighbor pairs, $J_{m(m\pm1)}$. GIXS reported values were used to set the inter site spacing values and total system dimensions to build the model monomer lattice.

2.2.1 Grazing Incident X-ray Spectroscopy determination of site spacing

The distance between the monomers along each of the axes in the crystal lattice was set in the model based on the empirical spacing measured by He *et al*.[43] The average intermolecular spacing was determined from reported Grazing Incident X-ray Scattering [GIXS] values (Table 1). GIXS was used because the low crystallinity of the lab grown PDBD-T-2F hinders transmissive X-ray crystallography analysis.[44-48] While GIXS is less precise than X-ray crystallography, diffraction measurements help describe the average conditions for low crystallinity blended systems.[49,50,66] GIXS measures the surface scattering effects of solid state systems to determine the D-spacing, *i.e.* the spacing between sites in the crystal lattice. GIXS also estimates the total crystal size defined as the crystal coherence length [CCL] based on the scattered peak shape per the Scherrer equation.[46] As the size of the crystal changes, its diffraction effects influence the scattering caused by the packing D-spacing and change interference strength affecting perceived out-of-phase minimum. This is why CCL is a function of the measured peak width.

Table 1: PDBT-T-2F approximate morphology as measured with GIXS[43]

System Axis	CCL [Å]	D-spacing [Å]
X, pi-stacking	29.58	3.56
Y, intra-lamellar	289.05	19.93
Z, down-chain	176.15	21.82

The PDBD-T-2F monomers were aligned in the model so that the pi-stacking between monomers occurs along the model's x-axis. The monomers were positioned with the down-chain backbone in the model's z-axis. The intra-lamellar interactions are along the model's y-axis (Figure 5). The transition dipole for every monomer was parallel and pointed in the down-chain direction. The yz plane of the model defines each lamellar sheet of PDBD-T-2F. Monomers are closest together in the pi-stacking direction while the intra-lamellar and down-chain distances are an order of magnitude further separated.

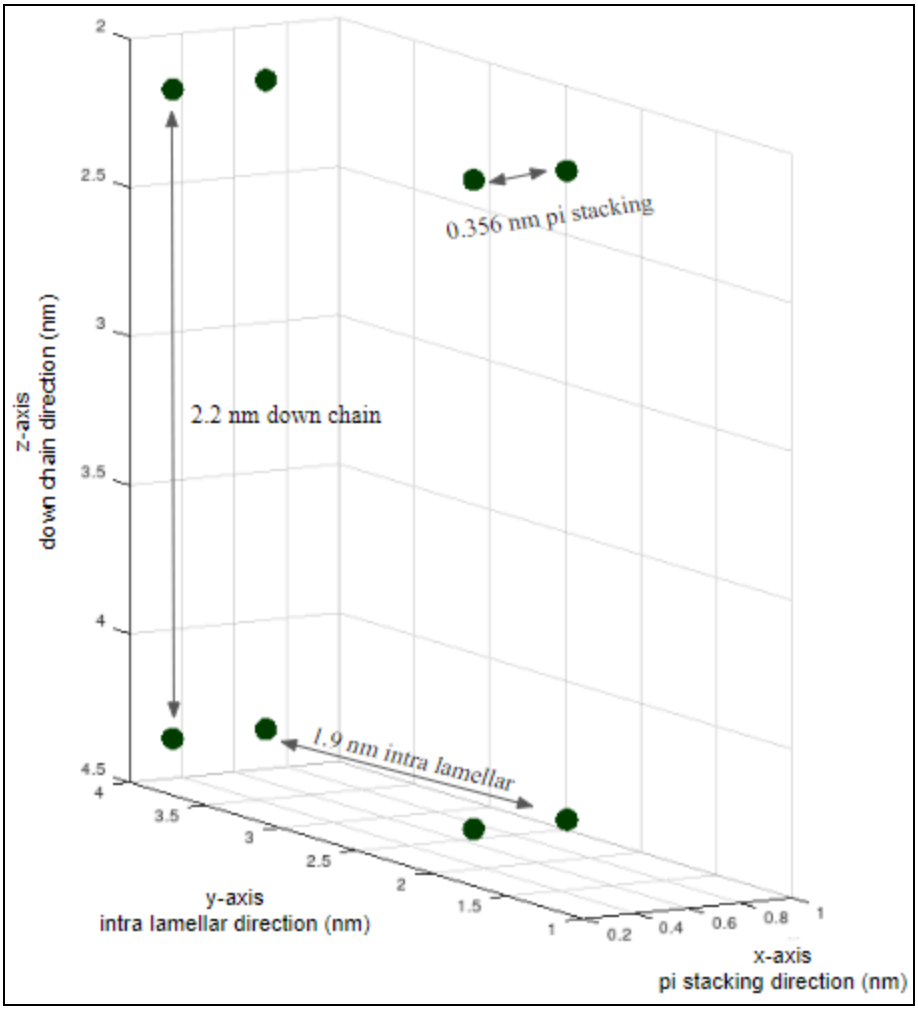

Figure 5 *Scaled PDBD-T-2F monomer sites as aligned in reference to the model axes. The center of each site is represented by a black circle. The model assigns the pi-stacking direction along the x axis, the intra-lamellar spacing along the y axis, and the down-chain direction along the z axis. DFT calculations were used for the coupling between these nearest-neighbor sites for each axis.*

The PDBD-T-2F representative crystal size results in 9 chains interacting in the pi-stacking dimension, 15 chains across the lamella dimension, and 9 repeating units aligned in the down-chain dimension (Equation 2).[51-54] This produces a crystal that is 2.958 nm × 28.9 nm × 17.615 nm in size.

$$\frac{CCL_i}{D-spacing_i} \simeq \ units\ across\ crystal\ dimension\ i \tag{2}$$

The GIXS calculated D-spacing for polymers is directly impacted by the side chain size. Larger non-conjugated alkyl groups increase the spacing in the lammela and pi-stacking directions.[54] The alkyl side chains of PDBD-T-2F may have a miniscule direct effect on the electronic properties, but they affect the overall geometry which can influence the overlap between pi systems. While there is research to modify PDBD-T-2F to enhance performance, He *et al.* measured the inter site spacing with an unaltered version of PDBD-T-2F, equivalent to the chemical structure used in this project's DFT calculations. The alkyl side chains were also included in the molecule structure for the DFT calculations to capture this potential effect. Additional study is needed to characterize the full effects of bulky side chains. Monomers with side chains exhibit a wide crystallinity variation because of how the side chain packs with neighboring side chains.[56] The change in morphology impacts the site to site coupling by changing the center to center distance as well as the alignment of the molecular rings changing the forces involved in exciton movement.

2.2.2 Density Functional Theory structure calculation

The transition dipole and excitation energy from the ground state to the first singlet excited state of one PDBD-T-2F monomer were calculated with density functional theory using Gaussian 16.[42] To speed up optimization of the ground state structure, a pre-optimization step was performed with the PM6 semiempirical method. The B3YLP functional and 6-31G basis set were used to reoptimize the structure (Figure 6a).[68] This refined structure was used in a time dependent density functional theory calculation to find the ten lowest singlet excited states of the monomer using the same functional and basis set as the ground state calculations. The HOMO and LUMO for the lowest singlet excited state are very delocalized along the backbone length (Figure 6b). These orbitals visually suggest the point dipole approximation (Section 2.3.1) may be inaccurate for the resulting delocalized transition dipole. The excitation energy for the lowest

singlet excited state of the PDBD-T-2F monomer was ε = 2.31 eV and the corresponding transition dipole magnitude was $|\hat{u}|$ = 3.68 D

The site energy, ϵ, was employed as the on-diagonal values for the site basis Hamiltonian, modified by a random gaussian site noise parameter, σ (Equation 1).

The transition dipole magnitude, $|\hat{u}|$ was used in the line dipole coupling calculation, described in Section 2.3.1 (Equation 4a). In this model, the transition dipole vectors were all set to align along the polymer backbone. There was no noise applied to the magnitude or orientation in the model. With this simplified model of the transition dipole, the coupling between each pair of sites was only affected by their relative geometry and the overall transition dipole magnitude parameter.

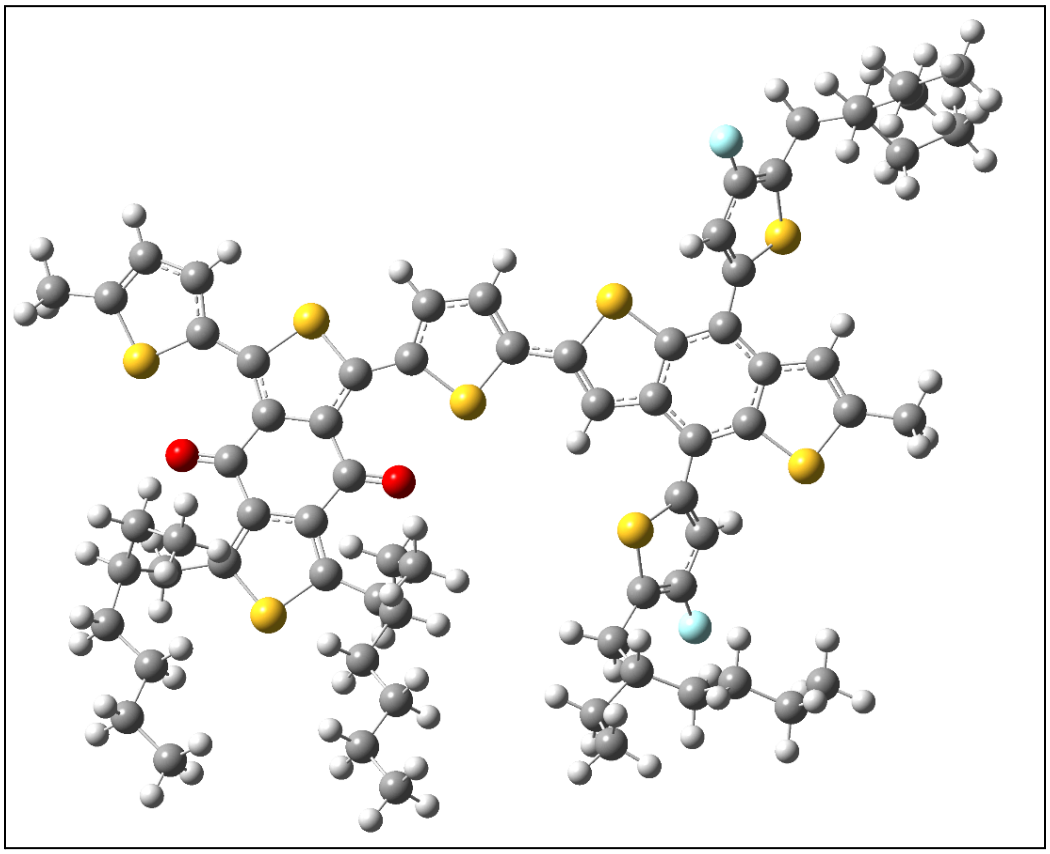

Figure 6a *Optimized geometry at the B3LYP/6-31G level for the PBDB-T-2F monomer with methyl end groups.*

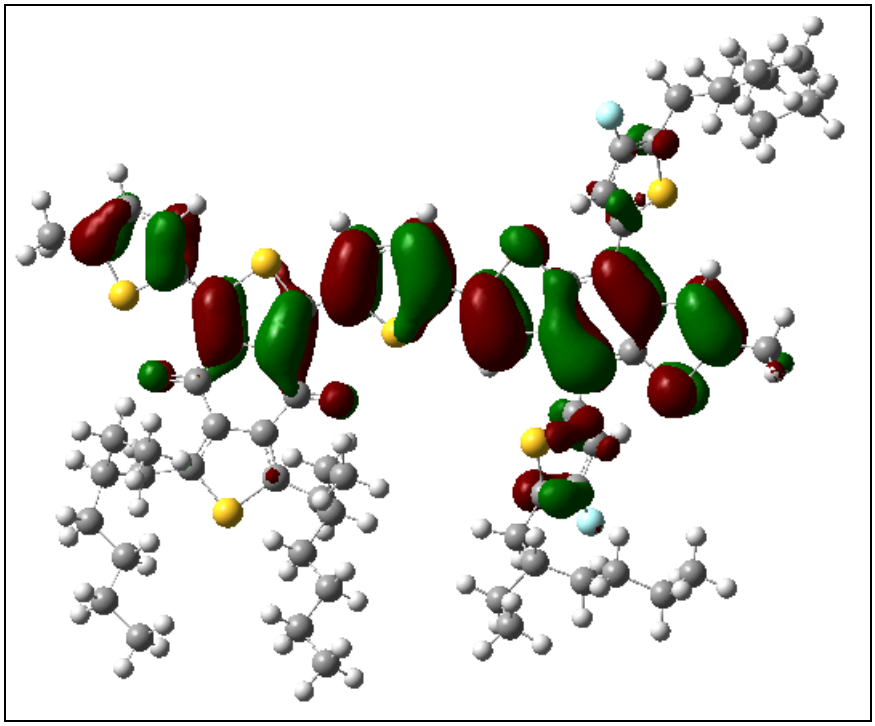

Figure 6b *HOMO and LUMO molecular orbitals for PDBD-T-2F monomer lowest singlet excited state for the B3LYP/6-31G optimized geometry. The delocalized orbitals visually indicate the point dipole approximation is a poor representation of the spread out transition dipole.*

2.3 Electronic coupling calculations

There are multiple options available to calculate electronic coupling including the point dipole approximation, the line dipole approximation, and DFT-based methods. As a highly simplified option, the point dipole approximation is the fastest calculation to use. However, its accuracy decreases when coupled sites are close together because it does not account for the size and shape of the coupled sites. The line dipole approximation requires more intermediate calculations than the point dipole, but the line dipole is more accurate for coupled sites that are close together because it accounts for the length of interacting sites. DFT calculations are more accurate than the line dipole approximation at the closest site spacings but require a large increase in computation time and complexity.

In this project, DFT calculations were used for the coupling values between immediately neighboring sites (Figure 5). These nearest-neighbor sites have inter site spacing similar to the length of the individual PDBD-T-2F monomers in the model. For all other, further separated sites in the model, the line dipole method was used to calculate the coupling values. This line dipole method provides sufficient accuracy to make physically relevant predictions while offering substantially reduced computer runtime. The point dipole method was not used, as the line dipole's runtime was acceptable with the benefit of increased coupling accuracy. The point dipole method is still beneficial to describe as a benchmark for the newly implemented line dipole method in this project.

2.3.1 Point dipole coupling approximation

The point dipole coupling approximation is a simplification of the Coulomb integral that assumes each transition dipole, μ, is entirely localized at the geometric center, r, of each site. With this simplification, the coupling, J_{mn}, between the sites, m and n, is calculated using equation 3.

$$J_{mn} \approx \frac{\mu_m \bullet \mu_n}{|r_m - r_n|^3} - 3\frac{[\mu_m \bullet (r_m - r_n)][\mu_m \bullet (r_m - r_n)]}{|r_m - r_n|^5} \quad (3)$$

This point dipole approximation erroneously overestimates the coupling when the inter site distance is the same or smaller magnitude than the length of the sites.[40] With the inverse relation between coupling and distance, at small inter site distances comparable to the site length, calculated coupling values rapidly increase. The overestimation occurs because the point dipole assigns the entire transition dipole to a single point while in reality it is distributed across the full length of the conjugated molecule. For extended systems this localization substantially increases the forecasted coupling interaction between close sites as shown below in Figures 9 and 12.

The point dipole approximation is not accurate for polymer matrices where the down-chain chromophore length is significantly longer than the distance between chromophores

in the directions normal to the chain. Beenken and Pullerits proposed a distributed line dipole model to more accurately calculate inter site coupling.[40]

2.3.2 Line dipole coupling approximation

The line dipole considers the dispersed nature of the long molecules' transition dipole by assigning fractions of the transition dipole across the length of the molecule. With the site's dipole divided across several locations on the site, a point dipole is calculated for each sub-coupling value between each location. The line dipole approximation is the sum of these sub-couplings. By subdividing the transition dipole this way, the length of the interacting sites is a factor in the coupling calculation, which is an advantage of the line dipole coupling approximation over the single point dipole coupling approximation (Figure 7).

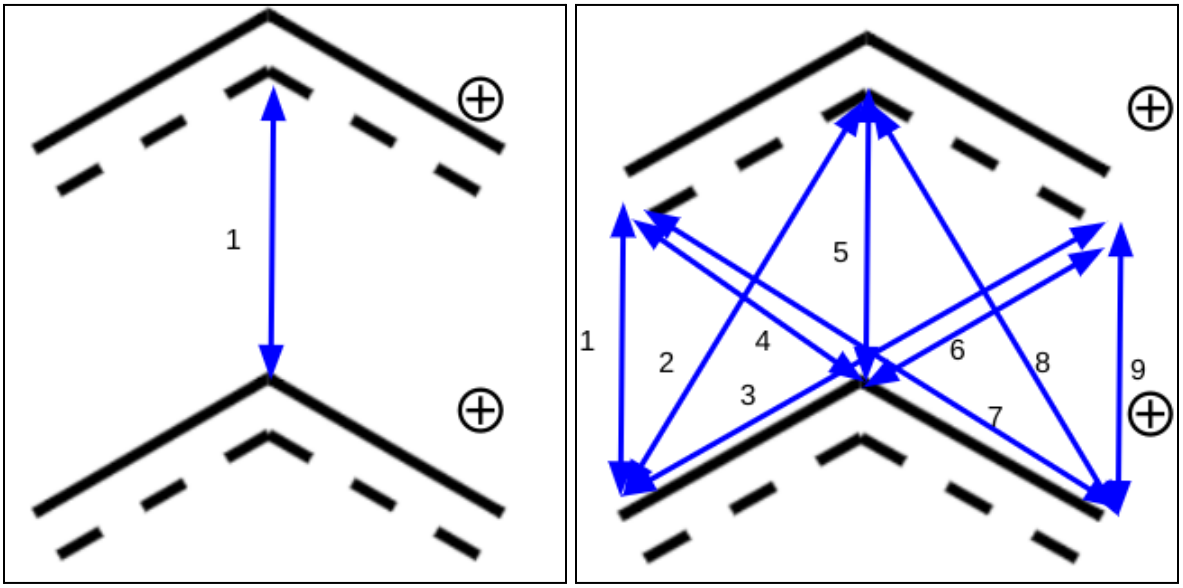

Figure 7 *Comparing the point and line dipole interactions for two allyl carbocations. (Left) The point dipole approximation assigns the entire transition dipole weight to the geometric center of each site. This produces 1 coupling value between each site. (Right) This line dipole approximation breaks the transition dipole into 3 subdipoles that are spatially distributed down the conjugated site length. When each site is broken into 3 subsites. a total of 9 subcoupling values are set between each site, which are then summed to produce the total coupling.*

To use the line dipole method, the site positions must be further divided into a user-decided number of subfractions. The total transition dipole magnitude for the site must then be distributed across each of these distinct subfraction positions. In this model the subfraction positions were set as evenly spaced points distributed over the down-chain length of the PDBD-T-2F monomer. The dipole magnitude of each monomer, μ_i, must be divided between each subsection $\mu_i^{(x)}$. A sinusoidal weighting distribution is used to assign more of the dipole magnitude to the central subfraction positions and less to the end subfractions (Equation 4, Figure 8).[40]

$$\mu_i^{(x)} = \mu_i \times \frac{sin(kx)}{\sum_x sin(kx)} \tag{4a}$$

k converts subfractions to radians as defined in 3b

$$k = \frac{\pi}{L+1}\text{; L=number of subfractions} \tag{4b}$$

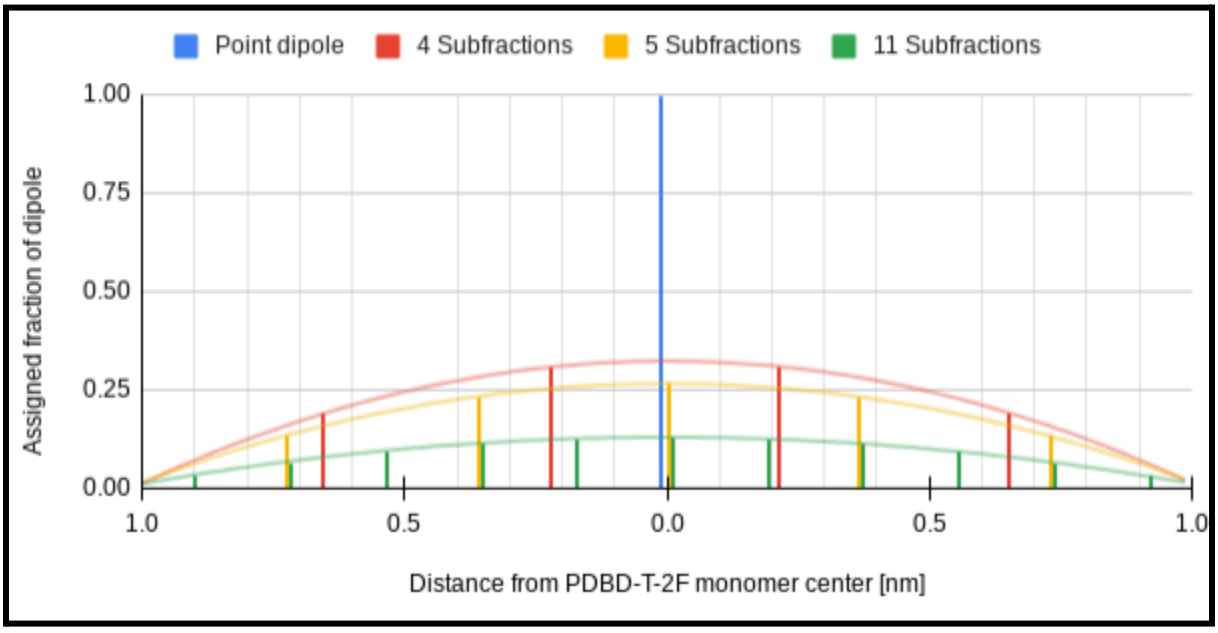

Figure 8 *The line dipole method sinusoidally weights the site dipole across each subfraction so more of the dipole is assigned to the central subfractions and less of the dipole is assigned to the edge subfractions.*

The line dipole requires less computational power than more detailed methods like the transition density cube method or full *ab initio* calculations while still improving the accuracy of the calculations over the point dipole approximation.[41] These more rigorous methods would reduce the size of the systems that can be studied in the same amount of computing time.

Increasing the number of subfractions in the line dipole increases accuracy, but also increases the computation time. Five subfractions for the target PDBD-T-2F model sizes was identified as an effective compromise between the increased accuracy of the coupling values for the nearby monomers and the modestly longer computation time required. Figure 9 compares the calculated coupling values for a pair of pi-stacked PDBD-T-2F monomers spaced 0.781 nm apart, which is the distance between the second closest pair of monomers aligned in the pi-stacking direction. The coupling values were calculated with the point dipole and line dipole approximations with varied numbers of subfractions. These coupling values were compared against the DFT coupling values. With an increasing number of subfractions, the line dipole approximation quickly converged toward the DFT result.

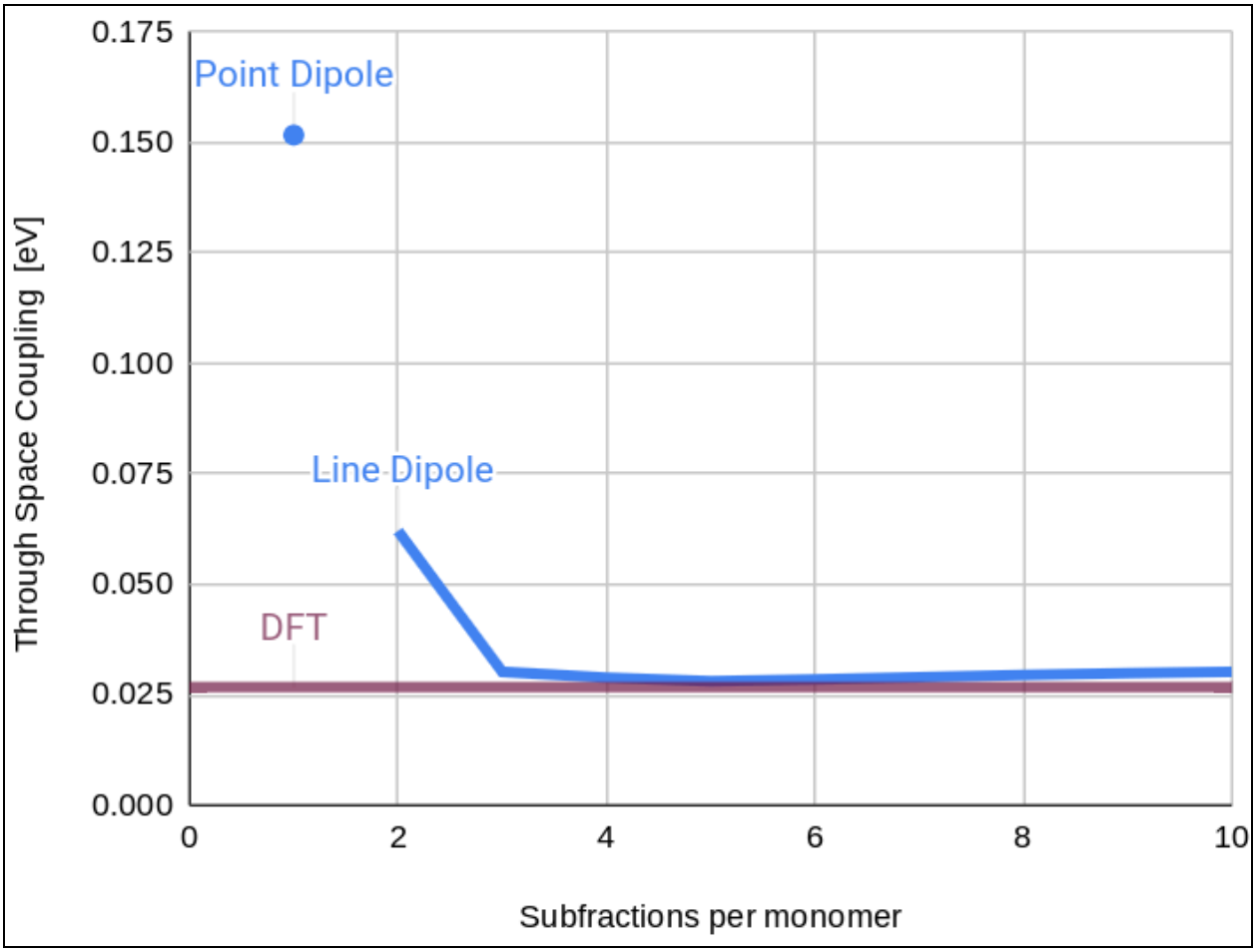

Figure 9 *The coupling values were plotted for two sites aligned 0.712 nm apart in the pi-stacking direction. Increasing the number of subfractions used improves the calculated coupling values for these 2nd closest monomers versus the DFT couplings. In the pi-stacking direction the coupling decreased from the point dipole to the line dipole and as more subfractions were used. The line dipole changes the coupling values less versus the point dipole values in the intra-lamellar and down-chain stacking directions where the sites are spaced further apart (Data not shown).*

Figure 9 shows the pi-stacking coupling values because the pi-stacking coupling is two orders of magnitude greater than the coupling in the intra-lamellar and down-chain directions, due in part to the closer spacing between the sites in the pi-stacking lattice dimension. For the

second closest pairs, the line dipole method still slightly overestimates the coupling values for the intra-lamellar and down-chain orientations versus the DFT calculation.

At further inter site spacing, the line dipole method and point dipole methods should converge as the distributed dipole in the line dipole method becomes less impactful as the relative length between coupled sites increases.[40] This expected property of the line dipole method was confirmed using a system of two poly(3-hexylthiophene-2,5-diyl) [P3HT] chains (Figure 10). The line dipole and point dipole calculated couplings converged as the inter site distance approached the length of the P3HT polymers. As recommended by Barford, packing distances less than twice the chain length dimension lead the point dipole to unacceptably overestimate the coupling thus favoring implementation of the line dipole method.[39]

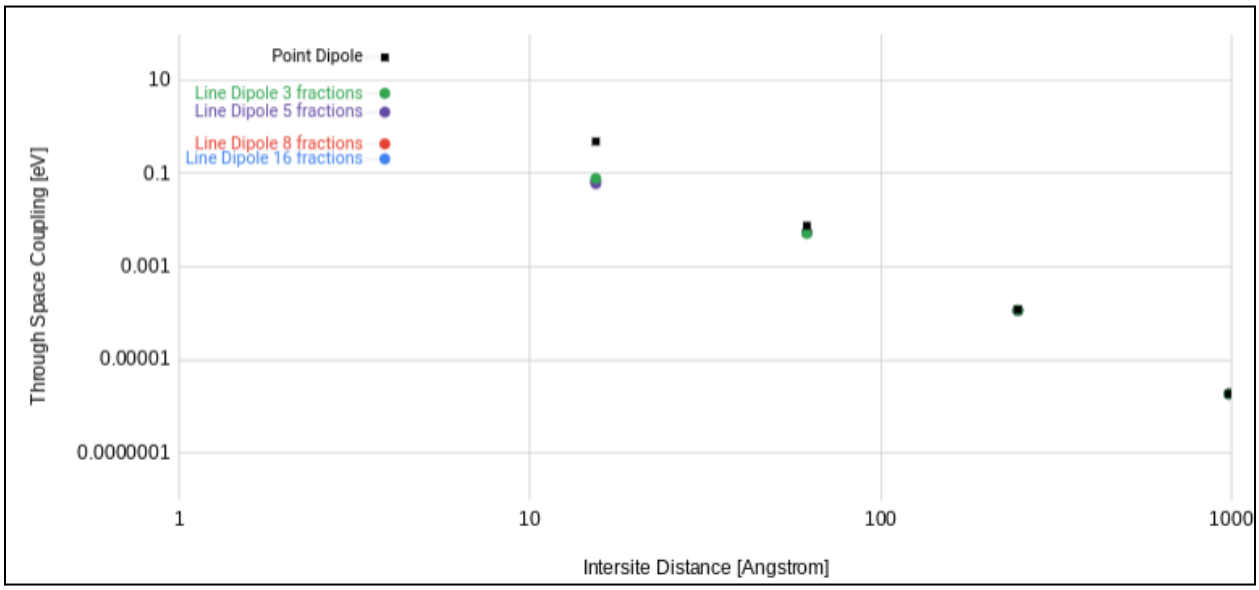

Figure 10 *The point dipole method coupling value converges toward the line dipole methods' as the distance between the sites increases. This behavior was modeled with 16-mer P3HT oligomers which are 61 Å long. The excitation energy and dipole strength values for the 16-mer P3HT were provided by Jacob Wat's prior research.*

When using the line dipole with small monomer sites, there is a slight risk the calculated coupling is less accurate for neighboring sites in the down-chain direction compared to the point dipole. This inaccuracy is because the increasing the number of subfractions, for sites aligned in the down-chain direction, moves the nearest-edge subfractions closer to the other site. Figure 11 illustrates this potential problem using two allyl carbocation sites aligned in the down-chain direction. The point dipole coupling uses the center to center distance as denoted with the blue arrow on the left. However, some of the line dipole subcoupling values use a shorter distance as denoted by the blue arrow on the right. The close spacing for some line dipole subcouplings can cause the total coupling to be overestimated.

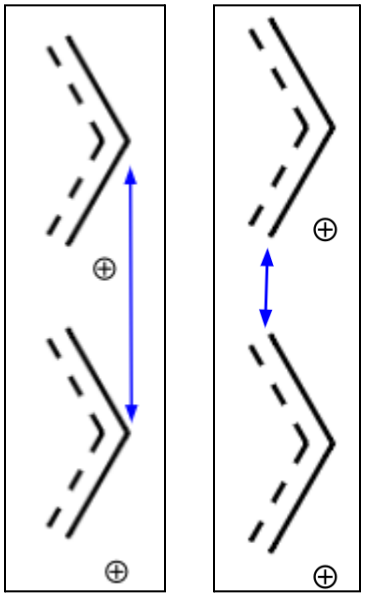

Figure 11 *Sites aligned in the down-chain direction can have some shorter coupling distances than the point dipole calculation on the same system. (Left) The point dipole approximation uses one inter site distance equal to the site spacing. (Right) The line dipole approximation uses multiple inter site distances, which can include distances that are shorter than that used in the point dipole approximation. Shorter calculation distances for both models risk overestimating coupling between sites.*

While these exterior subfractions have a smaller weighting factor than the central subfractions, their decreased distance would cause the line dipole to overestimate the coupling in the model for the closest spaced down-chain sites (Figure 12). For the monomer based model of PDBD-T-2F used in this project, the down-chain coupling between closest neighbor sites would have been drastically overestimated. For this reason, the coupling between the closest down-chain neighboring sites were set to the values calculated with DFT instead. Calculation of the DFT coupling values is explained in section 2.3.3 below. While the line dipole adds the most value modeling very long polymer chains because their transition dipole is spread out across their conjugated system, it still does greatly improve the monomer model accuracy when used for the second closest coupled sites.

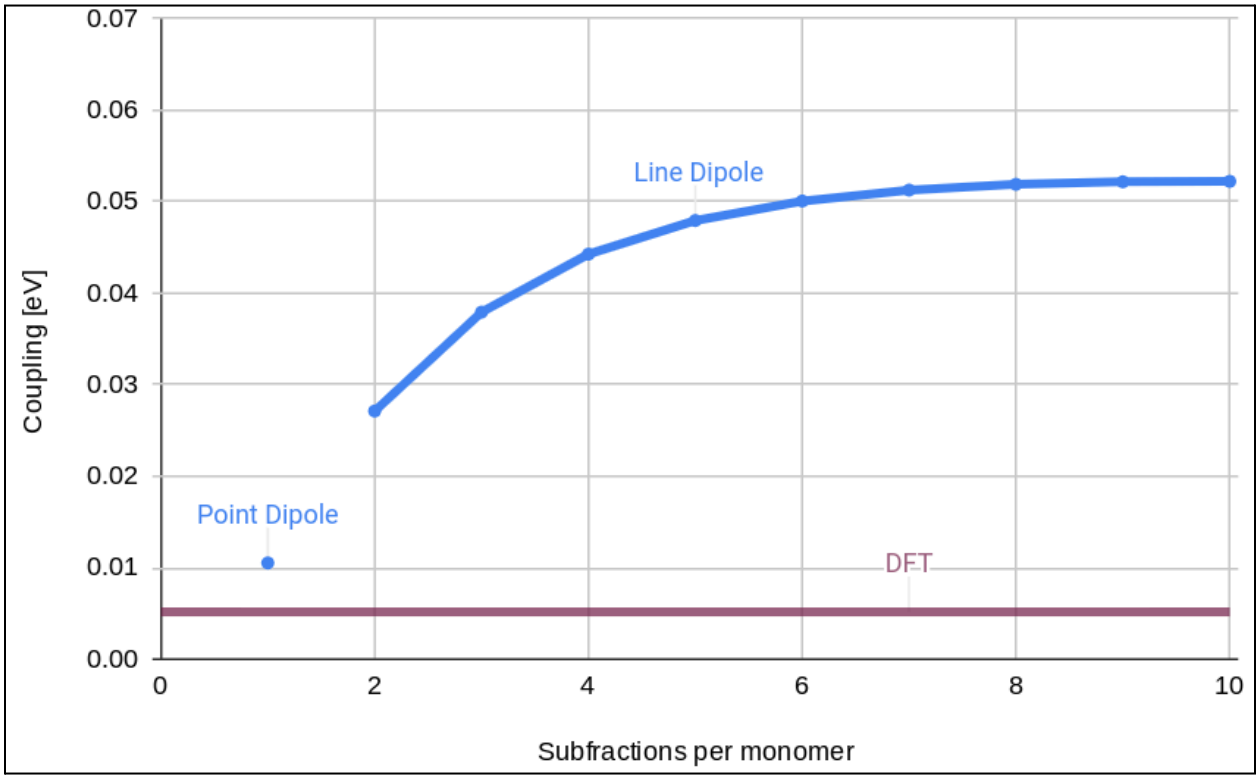

Figure 12 *For the closest down-chain neighbor sites 2.2 nm apart, the line dipole method overestimates coupling with increasing error versus the DFT calculation as the number of subfractions increases.*

As the line dipole is implemented in this code, each site is divided into the same number of subsites. This method creates a uniform number of subsites but would have non-uniform distance between subsites for a model that uses different sized oligomer repeating units. From an implementation standpoint, the consistent number of subsites is beneficial because the projected computation time and storage requirements can be forecasted before the model runs. However the constant number of subsites prevents anticipation of the minimum distance between subsites. This could be a concern because when two sites are less than two times the monomer spacing, the line dipole may be insufficiently accurate.[39] The additional complications should be weighed against the potential value should this line dipole method be used in the future to model a polymeric system with varied polymer lengths.

In an effort to use the most accurate available coupling values, DFT calculations were used to set the coupling for the closest site interactions in place of the line dipole approximation. The line dipole approximation was then only evoked when the sites are sufficiently spaced apart to enable accurate results.[39]

2.3.3 DFT coupling calculation

Density functional theory methods are *ab initio* calculations that can optimize the geometry of a chemical system and calculate its electronic structure. The generated electronic structure can be used to calculate coupling between sites as described below. This computational chemistry method produces more accurate results than the point and line dipole approximations because it fully accounts for the shape of the electron density distribution in the coupled sites, rather than approximating these three dimensional shapes as singular points along the chain. The increased accuracy of the DFT method requires substantially more computation time than the point or line dipole methods so it is not practically accessible to use for all the couplings in the model.

DFT calculation of coupling builds on the structural optimization of the monomer used in the line and point dipole calculations, which also includes the ground state energy of the optimized geometry. A time-dependent density functional calculation was run on the monomer calculating the first ten singlet excited states. The energy difference between the lowest excited state from this calculation and the ground state energy defines $\Delta E_{monomer}$, which is the single molecule analog to the optical band gap of a bulk material.

A similar process was used for the closely spaced monomer pairs. While these pairs are not chemically bound to each other, their close spacing facilitates through-space coupling where the electronic properties of the pair are altered versus the isolated monomer. The pairs were simulated by hand-aligning two copies of the optimized monomer in accordance with the three nearest neighbor geometries within the model in the pi-stacking, intra-lamellar, and down-chain directions. The monomer's optimized geometry was used for each pair with the assumption that the neighboring monomer would not significantly change the optimized geometry. After the ground state energy was calculated for each pair, the first three singlet excited states were calculated to determine the band gap for each pair. For all orientations the singlet excitation energies with the highest oscillator frequencies were used. The coupling for the paired sites is defined as one half of the difference between the band gap of the monomer and the band gap of the pair as shown in Figure 13 and Equation 5.[2]

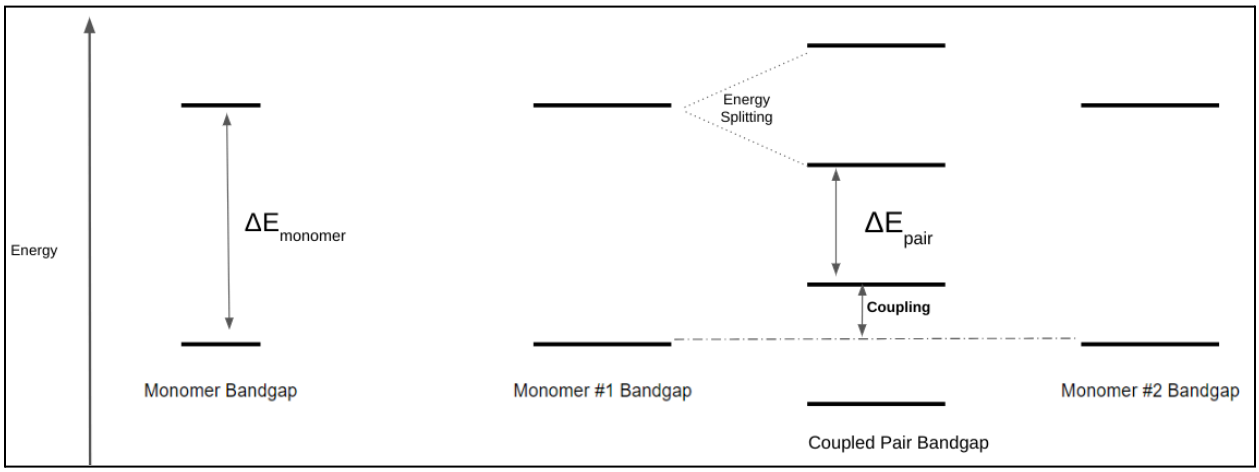

Figure 13 *Coupling between monomers in reference to the single monomer and pair's orbital excitation energies. Coupling equals half the energy difference between the monomer band gap and the pair band gap.*

$$J = \frac{1}{2}(\Delta E_{monomer} - \Delta E_{pair}) \quad (5)$$

The band gaps for all three axial packing neighboring pairs in the PDBD-T-2F crystal structure are: 1.89 eV in the pi-stacking orientation, 2.30 eV in the intra-lamellar orientation, and 2.29 eV in the down-chain orientation. The lower energy excitations for the pairs have a coupling of 0.21 eV in the pi-stacking direction, 0.0017 eV in the intra-lamellar direction, and 0.0052 eV in the down-chain direction.

2.4 Matrix transformation to the exciton basis

The Hamiltonian is built in the site basis as a combination of coupling energies between sites and site energies with a random noise component. Diagonalizing this Hamiltonian produces a transformation matrix, $\hat{U}$, composed of eigenvectors that map each eigenstate of the system onto the site basis. Diagonalization also reveals the eigenenergies of the eigenstates, which are combined as the eigenvalue λ (Equation 6a). The eigenbasis of the Hamiltonian, consisting of eigenstates representing delocalized excitons, is defined as the exciton basis in this model

(Equation 6b). These delocalized eigenstates are a good model of the expected energy absorption response for the modeled system.[63]

$$\widehat{HU} = \lambda\widehat{U} \tag{6a}$$

$$H_{exciton\ basis} = \widehat{U}^{-1} H_{site\ basis}\widehat{U} \tag{6b}$$

The density matrix, $\hat{p}$, is an ensemble-based representation of population in the model system. The density matrix is defined as a square matrix with dimensions equal to the number of sites in the system. In the site basis, the diagonal elements of $\hat{\rho}_{site\ basis}$ represent the fraction of population found at each monomer in the model. The off-diagonal elements, known as coherences, describe any existing superposition character of the excitation. In the site basis density matrix each off-diagonal entry describes the superposition of the excitation across two corresponding sites.

The density matrix can also be transformed into the exciton basis. In the exciton basis each diagonal element of $\hat{\rho}_{exciton\ basis}$ represents a delocalized eigenstate of the system, commonly referred to as an exciton. These excitons can be transformed into the site basis to show the probability they have to occupy physical sites in the model using the transformation matrix defined in the diagonalization procedure. (Equation 6c).

$$\widehat{\rho}_{site\ basis} = \widehat{U}\widehat{\rho}_{exciton\ basis}\widehat{U}^{-1} \tag{6c}$$

Both the site basis and the exciton basis density matrices are useful starting points for the model simulations. The site basis density matrix can be used to define initial states in space that can be fully localized at a site or spread across several sites and these states can include superposition-based off-diagonal excitations as well. This position can be propagated through time to understand how the coupling affects exciton transport (Section 2.5). Selecting an initial state localized entirely on a single site offers a physically intuitive, albeit oversimplified, starting state. By selecting the initial position of excitation, the model can distinguish how the dynamic

behavior depends on the physical characteristics of the starting position, *e.g.*if one face is preferentially irradiated versus another.

When a simulation's initial state is defined in the exciton basis, the transformation matrix can map the delocalized character of this state into the site basis. When transforming the exciton basis initial states in this way, the resulting site basis density matrix shows a realistic physical distribution of excitation corresponding to the excited states created by photon absorption by the model system. Because each exciton is an eigenvector for the site basis Hamiltonian, each exciton's site basis density matrix is stationary through time in this time-independent Hamiltonian model.

Using the exciton basis density matrix allows one to study the excitation initial behavior and absorption spectrum (Section 2.6.1). There are an equal number of possible excitons and sites in the system. All of these excitons and their corresponding excitation energy must be analyzed as a set when producing absorption spectra or interpreting delocalization differences.

2.5 Time evolution of the exciton density matrix

The Liouville-von Neumann equation was employed to calculate time evolution of the ensemble of states for the model systems (Equation 7).[57] This time propagation was only conducted in the site basis using the Hamiltonian and density matrices in their site basis form. The dephasing parameter, γ, was added to simulate the eventual decoherence of quantum superpositions that is observed macroscopically. Mathematically, the parameter exponentially lowers the magnitude of the off-diagonal density matrix elements. These coherences describe the superposition character of the ensemble of states with larger values corresponding to more substantial delocalization between sites. In real systems, slight variations in oscillation frequency due to differences in the local environments between each site will drive the oscillating ensemble out of phase over time. The coherence reduction parameter γ was set constant at 3,000 cm^{-1} as a

reasonable estimate of the room temperature system-bath coupling, which sets the exponential lifetime for off-diagonal coherences around 30 fs.[58]

$$\frac{d}{dt}\hat{\rho} = -\frac{i}{\hbar}(\hat{H}\hat{\rho} - \hat{\rho}\hat{H}) - \gamma \quad (7)$$

To utilize the Liouville-von Neumann equation, the 4th order Runge-Kutta method was employed as a numerical solution to approximate the stepwise density change in time.[58] A small timestep of 0.1 fs was used to minimize the risk that the linearization of Equation 7 would deviate from the true behavior. An even smaller timestep could be used at the expense of increased computation time.

2.6 Model analysis tools

2.6.1 Visualization methods for spatial and spectral results

For site basis density matrix data, the spatial probability for the exciton can be plotted to more intuitively show where the exciton may be found rather than solely reading the matrix values. Figure 14 shows the visual representation of a site basis density matrix result. Figure 14 plots the scaled position of each site in the system with the pi-stacking dimension pointing out of the page, the down-chain dimension pointing up and down the page, and the intra-lamellar dimension pointing side to side. To improve the visual clarity, these axes are tilted slightly so circles representing the sites do not cover each other up in the two-dimension printout of the figure. Each circle is colored according to the exciton's probability to be found at that site. This circle color, quantified on the right hand side of the figure, follows a logarithmic scale with warmer colors corresponding to higher occupancy probability and cooler colors having lower probability of occupancy. Sites with less than 10^{-6} probability of occupancy are not shown to ease the visual interpretation of the most probable sites. The total crystal size of the simulated system is shown on the *x,y;z* axes scales.

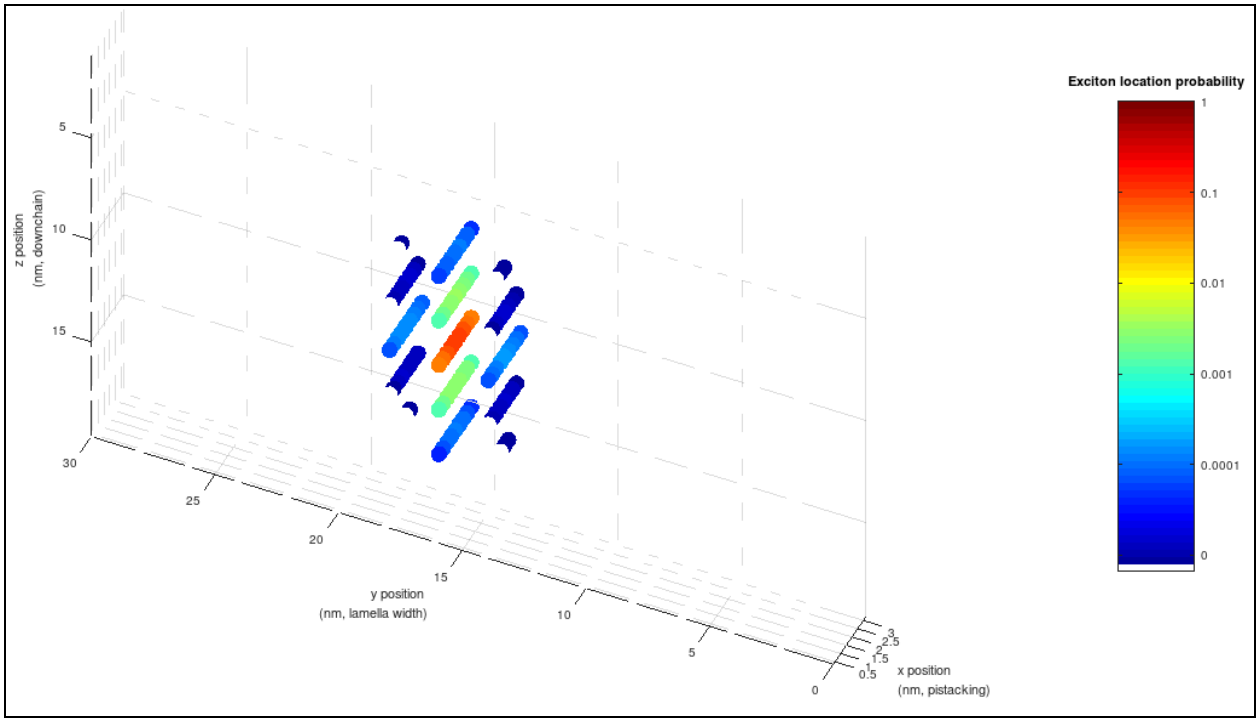

Figure 14 *Simulation of exciton delocalization from the center site in a 9x15x9 unit system after 10 fs. Delocalization is predominantly directed in the pi-stacking orientation with substantial occupancy of all sites that are pi-stacked with the center starting site. Conversely, delocalization in the intra-lamellar direction only extends one site to the closest monomers. Delocalization in the down-chain direction only extends two sites.*

While GIXS measurements report the average PDBD-T-2F crystal size is 9x15x9 unit in size across each dimension, the majority of the results to be presented in this project are displayed on smaller 9x5x5 unit systems. To efficiently study exciton behavior, it is useful to decrease the modeled crystal size in the lamellar and down-chain directions due to the substantially lowered coupling and consequently reduced exciton travel distances in these dimensions. As the exciton predominantly delocalizes in the pi-stacking direction due to the higher coupling in the pi-stacking direction, the extraneous lamellar and down-chain sites can be removed from the model to speed computation without reducing accuracy as demonstrated in the results Section 3.3.

This visualization framework allows qualitative evaluation of delocalization at each timestep when propagating the population density in the site basis through time. For example, Figure 15 includes two plots of the exciton spatial probability at different timesteps in the same system. In the first plot the probability is shown 1 fs after the population is initially set to completely occupy the central site. In the second plot the probability is shown 10 fs after the same initial state. Visually comparing the results quickly shows the clear increased delocalization after 10 fs compared to 1 fs.

This ease of analysis is in line with the goal of this model to improve simulation access for all researchers. Rather than necessitating time on a supercomputer, this faster model enables local computation. This visual tool supplements the model's flexibility by letting a scientist see which conditions are visually interesting and worthwhile to analyze quantitatively.

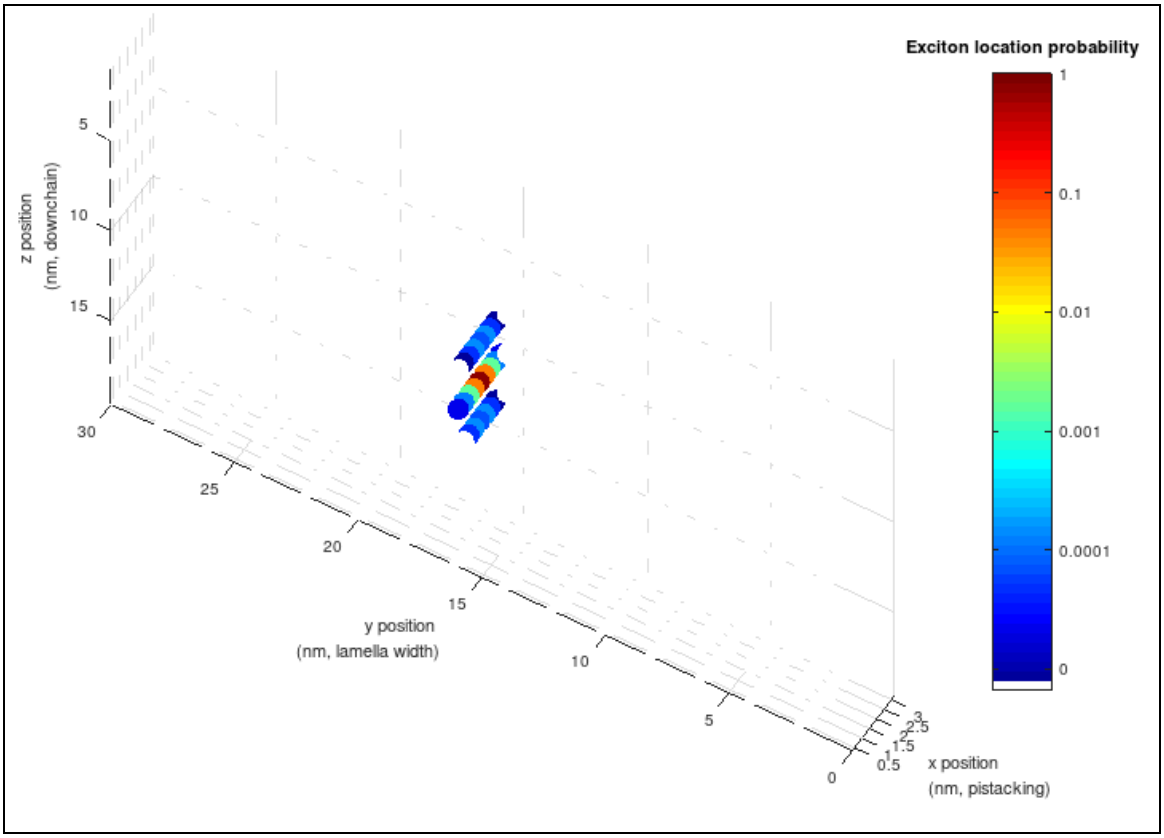

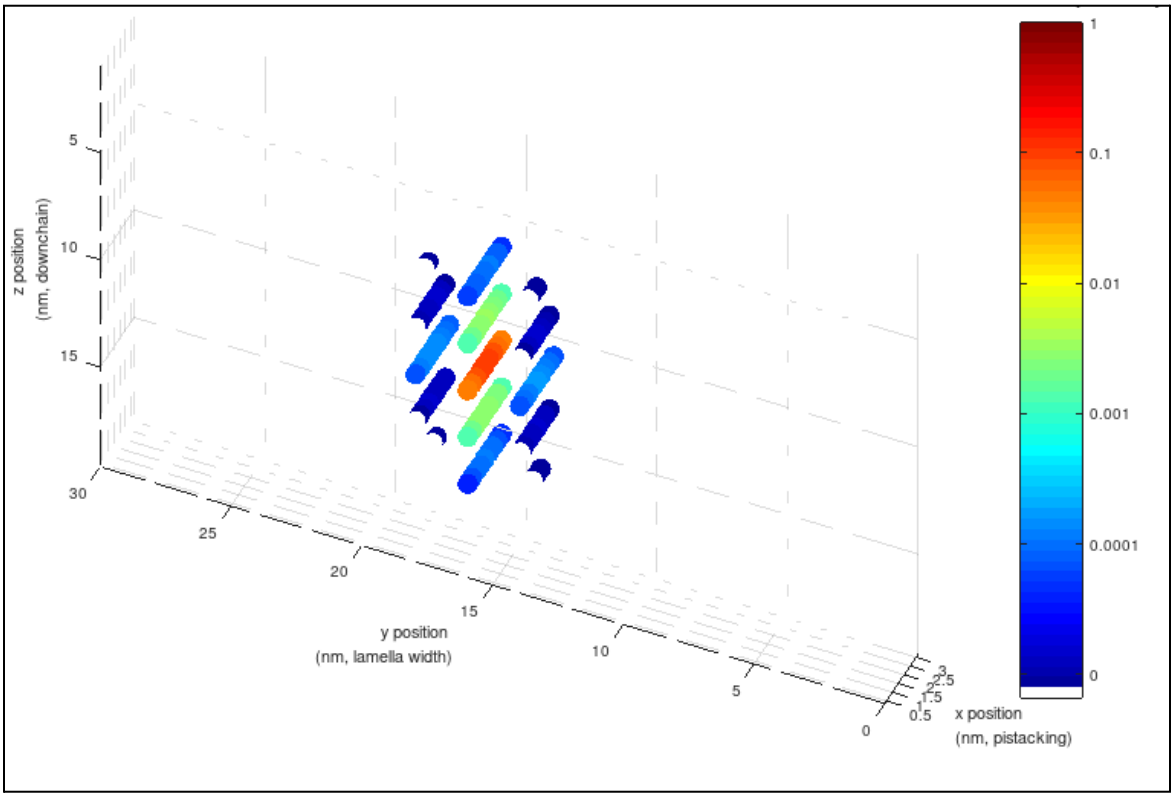

Figure 15 *Exciton delocalization through time after 1 fs (Top) or 10 fs (Bottom) when the exciton is set initially on the central site of a 9x15x9 unit system. After 10 fs the exciton delocalized more in all three directions.*

The excitation energies, which are produced by the diagonalization of the site basis Hamiltonian, are used along with an empirically set convolution width to create the predicted absorption spectra of the modeled systems. After the site basis Hamiltonian matrix is built, it is diagonalized to convert it from the site basis into the exciton basis where the diagonal elements define the excitation energies for each eigenstate (Equation 6b).

The absorption spectrum of the system is modeled as a weighted sum of normal distributions centered at each eigenenergy (Equation 8). In principle these peaks are weighted according to the transition dipole for the site along with the transformation matrix. In the implementation for this project, the weighting procedure has no effect because every site is identical in size with the same transition dipole magnitude. If the diagonalized Hamiltonian has more eigenstates of a specific excitation energy, it follows that the system will display a higher absorption of incoming light at the corresponding wavelength. The coupling energy dependence is modeled with a normal distribution applied to the stick spectrum because experimental measurements have finite linewidths.

$$Abs(x) = \sum [|\hat{u}| * U]^2 * e^{-2.772(\frac{x-\mu}{\sigma})^2} \quad (8)$$

$\hat{u}$ = excited dipole, U = righthand eigenmatrix,

2.772 = Debye to eV conversion factor[59], $\boldsymbol{\sigma}$ = convolution width

A convolution width ($\boldsymbol{\sigma}$) up to 0.25 eV is employed to represent the total peak broadening effects in the system. Doppler broadening is expected to be the largest contributor to broadening at room temperature for condensed matter. This Doppler broadening is due to the variance in the local environment for each site and is represented previously in this model in Equation 1 as σ. Line broadening due to coupling strength is another process which broadens real spectral peaks that is inherently included in this model in the eigenenergy distribution.[60,61]

These broadening effects were explored by varying the convolution width variable for a constant Hamiltonian. As convolution width increased, the peaks started to blend together, reducing the number of distinguishable peaks. At 0.25 eV, this blending also smoothed the absorption profile so all energies between the band gap and highest eigenenergy displayed substantial absorption relative to the spectrum produced with a lower, 0.05 eV convolution width (Figure 16).

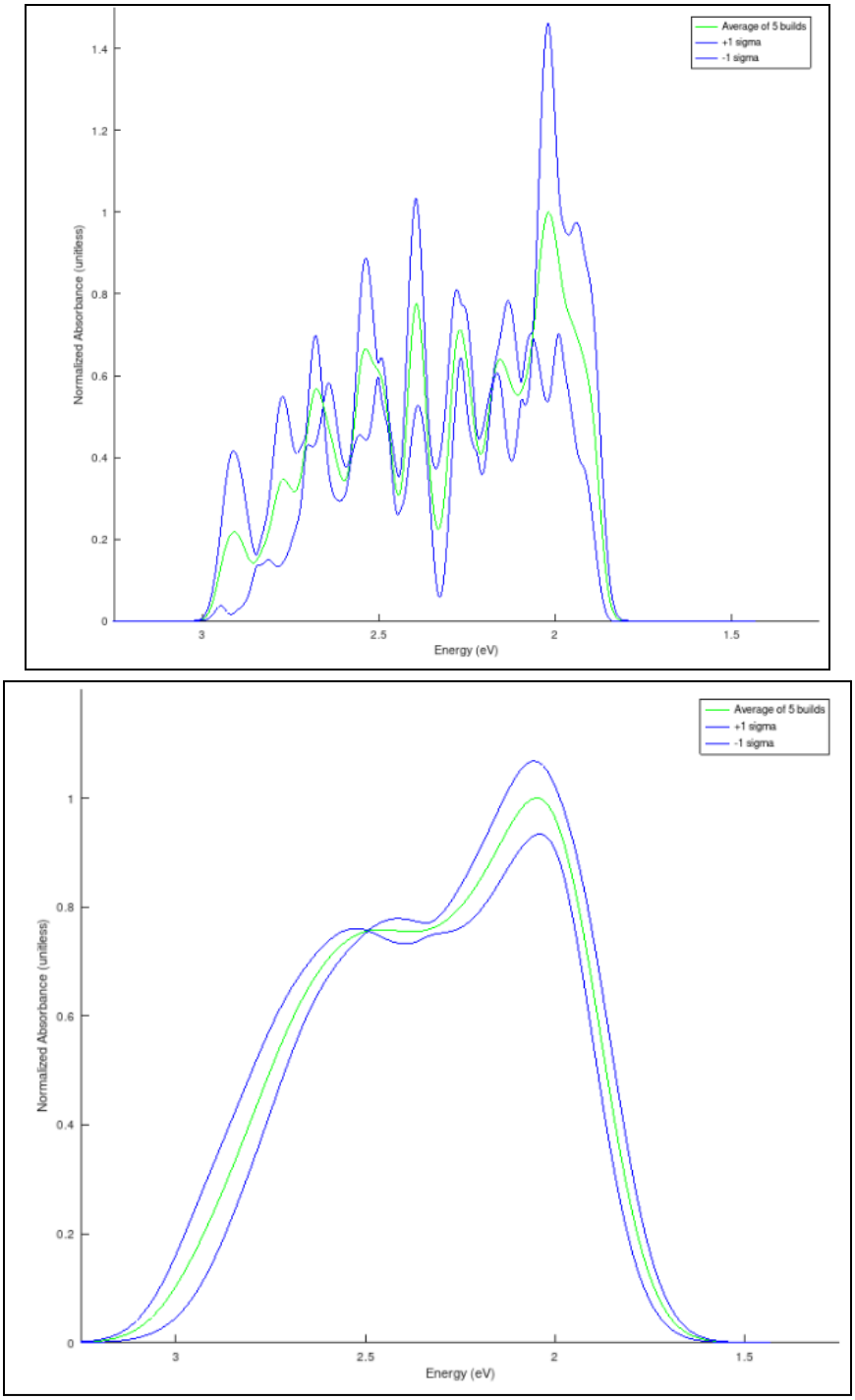

Figure 16 *(Top) For a system with 9x5x5 units, a convolution width of 0.05 eV leaves distinguished peaks. (Bottom) For a system with 9x5x5 units and a convolution width of 0.25 eV the peaks blend together. The peaks in the modeled spectrum for a PDBD-T-2F system are smoothed when convolution width increases. Figures show the averaged absorption spectra of 5 repeated simulations to build the Hamiltonian matrix.*

2.6.2 Participation ratio index to quantify delocalization

For a given system, the extent of exciton delocalization can be quantified using a participation ratio [PR()] index (Equation 9).

$$PR() = \frac{1}{\sum_{i=1}^{total\ sites} \rho_{ii}^{2}} ;\ the\ site\ basis\ \rho\ matrix\ is\ used \quad (9)$$

The PR() index ranges from 1 to the total number of sites in the system. A value of 1 means the exciton population is entirely localized on one site. A value equal to the number of sites means the population is distributed evenly across all sites in the system. As delocalization is vital to spread central excitons toward domain boundaries, a higher PR() index value suggests a system may be more likely to spread population to the edges of the domain to achieve charge transfer. The average, variance, and relative standard deviation of the PR() index are useful in the interpretation of the system behavior. Because the range of PR() varies with system size, the relative standard deviation offers a rough normalization option so larger systems can be compared against smaller sized systems.

Section 3: Results & Discussion

3.1 Effects of pi-stacking on simulated absorption spectra and PR() index

Coupling in the pi-stacking direction is the predominant driver affecting system eigenenergies used to produce the simulated absorption spectra. A lower line broadening value (0.1 vs 0.25 eV) was used to generate the Figure 17 spectrum to enhance resolution and clearly show the pi-stacking effect.

For a system without pi-stacking sites, the absorption spectrum has a unimodal distribution centered at the monomer excited energy of 2.31 eV. This roughly symmetric peak has an average PR() value of 1.4 with a standard deviation of 1.2 (Figure 17a). This low PR() value results from the smaller number of sites (25) in the system as well as the diminished delocalization between the sites.

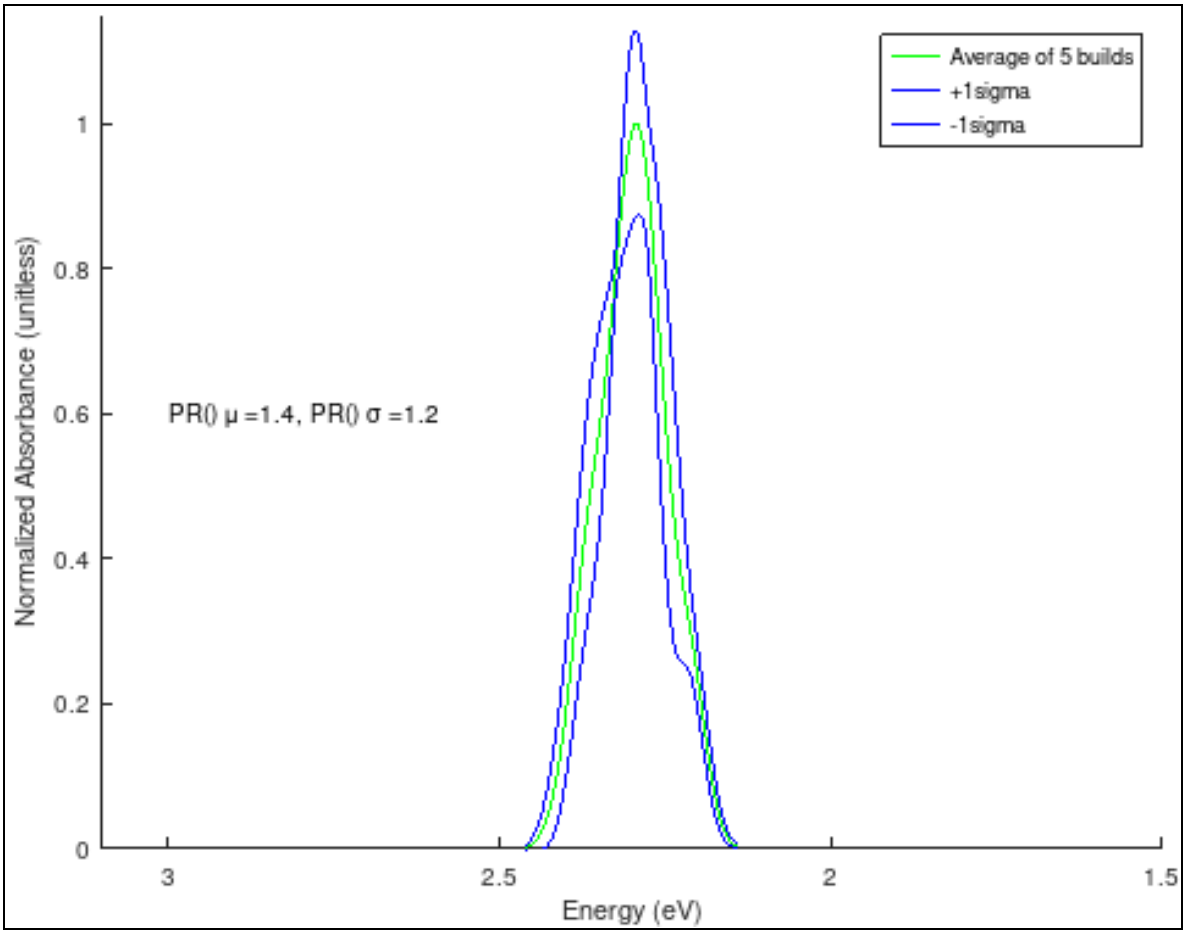

Figure 17a *Averaged absorption spectrum of 5 repeated simulations of a 1x5x5 unit system. The site energy noise has a standard deviation of 0.05 eV and the peak convolution width is set at 0.1 eV. No pi-stacking coupling is available in this single lamella sheet geometry. Spectra are normalized by assigning the energy with the largest average absorption a value of 1 and applying this scaling factor to all other absorption values across the energy range. The system has a PR() average of 1.4 with a standard deviation of 1.2.*

For systems with multiple lamellar sheets arranged in a pi-stacking orientation, the coupling between neighboring monomers creates additional peaks in the 2x5x5 unit system absorption spectrum. For a pair of lamellar sheets, each site is oriented facilitating pi-stacking with one other site in the system. Figure 17b shows the distinct absorption spectrum resulting from this change in available coupling interactions. Rather than a single peak centered at 2.31 eV, the system with two lamellar sheets has two absorption peaks centered at 2.5 and 2.1 eV. The

asymmetry of both peaks suggests there are multiple closely spaced eigenstates within each peak that are not resolved. With more sites in the system and increased delocalization between sites, the PR() average greatly increased to 9 for the high-energy peak and 5 for the low-energy peak for this 2x5x5 unit system. The standard deviation for the PR() values between eigenstates moderately increased to 4 and 2, respectively, for the high and low-energy peaks.

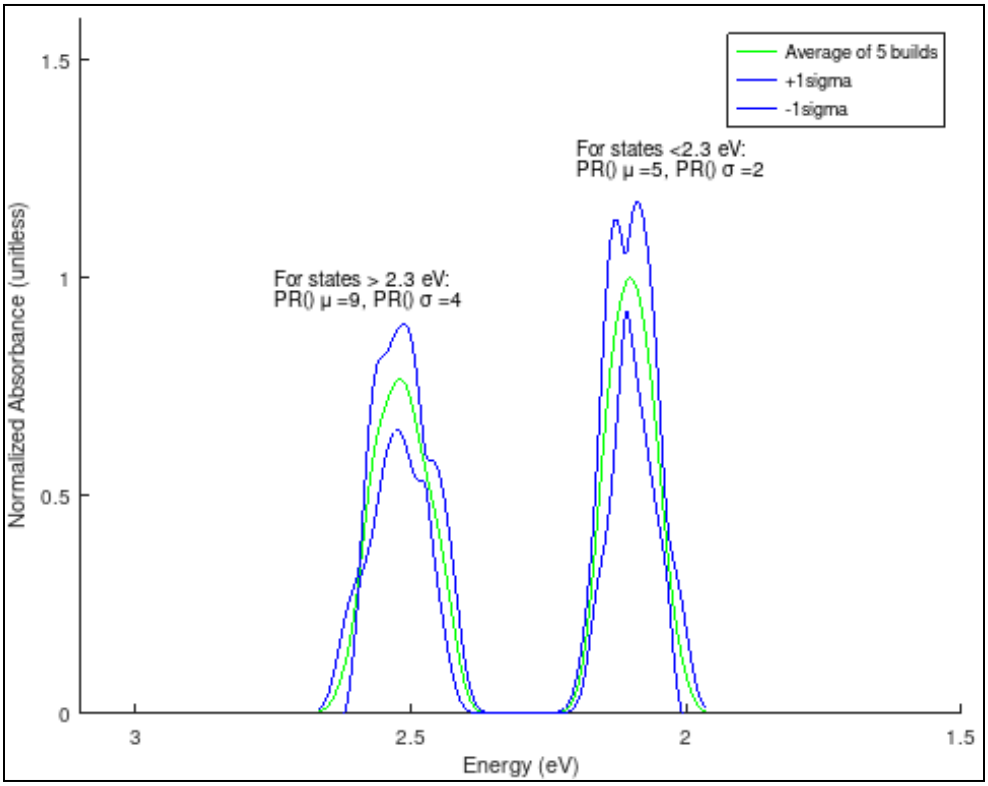

Figure 17b *Averaged absorption spectrum of 5 repeated simulations of a 2x5x5 unit system. The site energy noise has a standard deviation of 0.05 eV and the peak convolution width is set at 0.1 eV. Spectra are normalized by assigning the energy with the largest average absorption a value of 1 and applying this scaling factor to all other absorption values across the energy range. The system eigenenergies greater than 2.3 eV have a PR() average of 9 with a standard deviation of 4. The system eigenenergies less than 2.3 eV have a PR() average of 5 with a standard deviation of 2.*

The nearest neighbor pi-stacking monomers have a coupling strength of 0.21 eV. The behavior is aptly modeled in the 2x5x5 unit monomer system with two distinct absorption energy levels at 2.1 and 2.5 eV, approximately shifted ±0.21 eV from 2.31 eV, the monomer excitation energy. The missing absorption peak at 2.31 eV suggests that the exciton for every eigenstate is coupled across both pi-stacked sites rather than localized at one monomer.

When a third lamellar sheet is added in the 3x5x5 unit system still more new coupling interactions become available to change the energy levels and simulated absorption spectrum. As shown in Figure 17c, new absorption peaks appear at 2 and 2.6 eV. The peak near 2.31 eV also reappears when the 3x5x5 Hamiltonian is diagonalized, reminiscent of the monolayer system. The shifted high and low-energy peaks are explained by the additional lamellar layer that decreases the band gap between the HOMO and LUMO and increases the energy difference for the high-energy peak. The delocalization behavior is different for each of these peaks. The high-energy peak has the largest PR() values with an average of 17 and a standard deviation of 6. The peak at the site energy has the smallest PR() values with an average delocalization value of only 3 and a small standard deviation of 1.3 which are similar to the PR() values for the same energy peak in the 1x5x5 unit system. The low-energy band gap peak has a moderate average PR() value of 8 and standard deviation of 3. The increased delocalization at the band edge peak is a beneficial property of the system because it increases the likelihood low-energy excitons will delocalize to reach the system edge to be harvested.

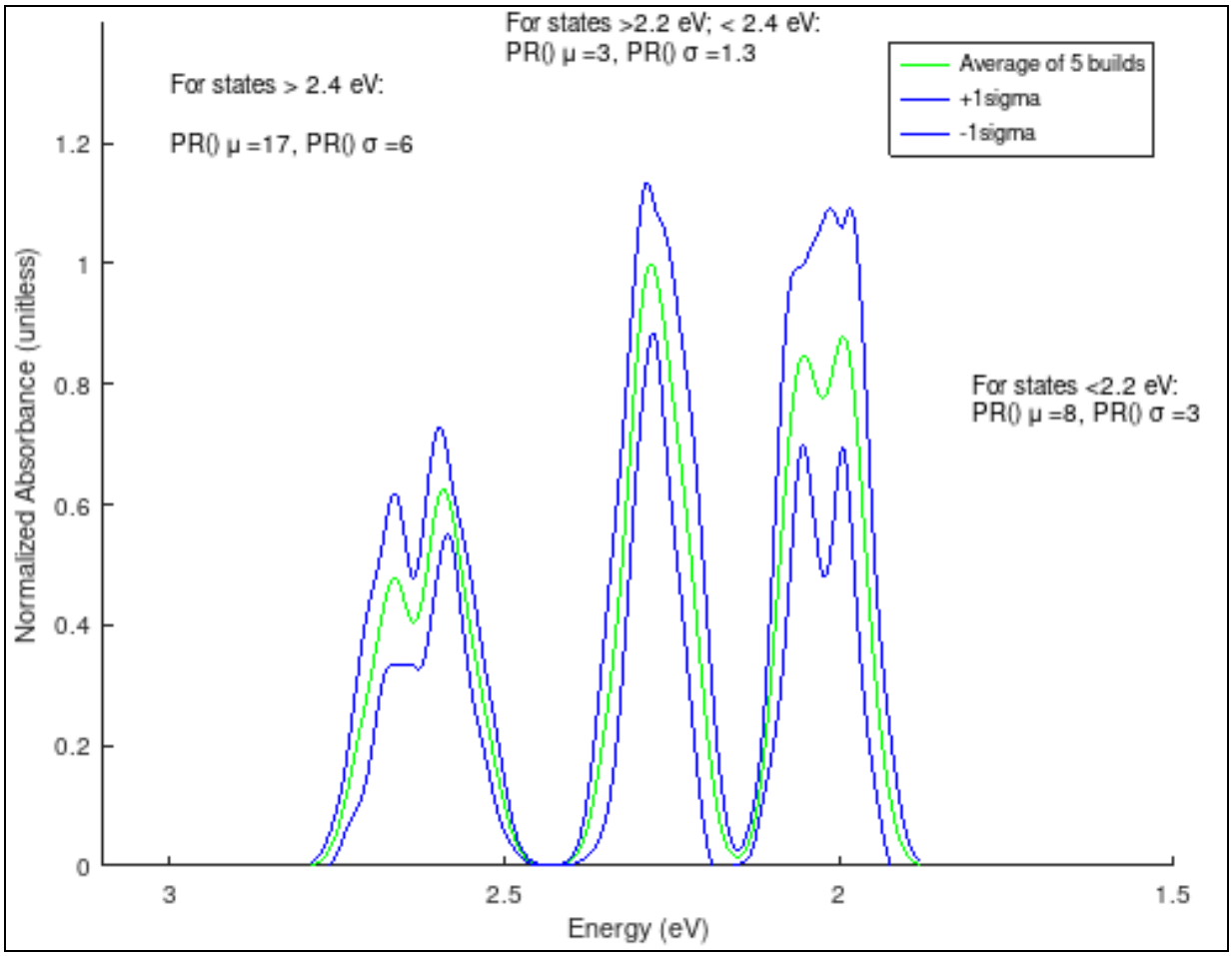

Figure 17c *Averaged absorption spectrum of 5 repeated simulations of a 3x5x5 unit system. The site energy noise has a standard deviation of 0.05 eV and the peak convolution width is set at 0.1 eV. Spectra are normalized by assigning the energy with the largest average absorption a value of 1 and applying this scaling factor to all other absorption values across the energy range. The system eigenenergies greater than 2.4 eV have a PR() average of 17 with a standard deviation of 6. The system eigenenergies between 2.4 and 2.2 eV have a PR() average of 3 with a standard deviation of 1.3. The system eigenenergies less than 2.2 eV have a PR() average of 8 with a standard deviation of 3.*

Additional lamellar sheets add complexity to the available and favorable interactions within the system. For the absorption of a 4x5x5 unit system as shown in Figure 17d, the high

and low-energy peaks spread in width and split into multiple nodes. The PR() trend continues with the high-energy peak set having the largest average PR() at 28 with a standard deviation of 10. The site energy peak had the lowest delocalization with a PR() average value of 6 and a standard deviation of 3. Compared to the site energy peak, the eigenstates of the low-energy peak set have increased delocalization with a PR() average value of 10 and a modest standard deviation of 5.

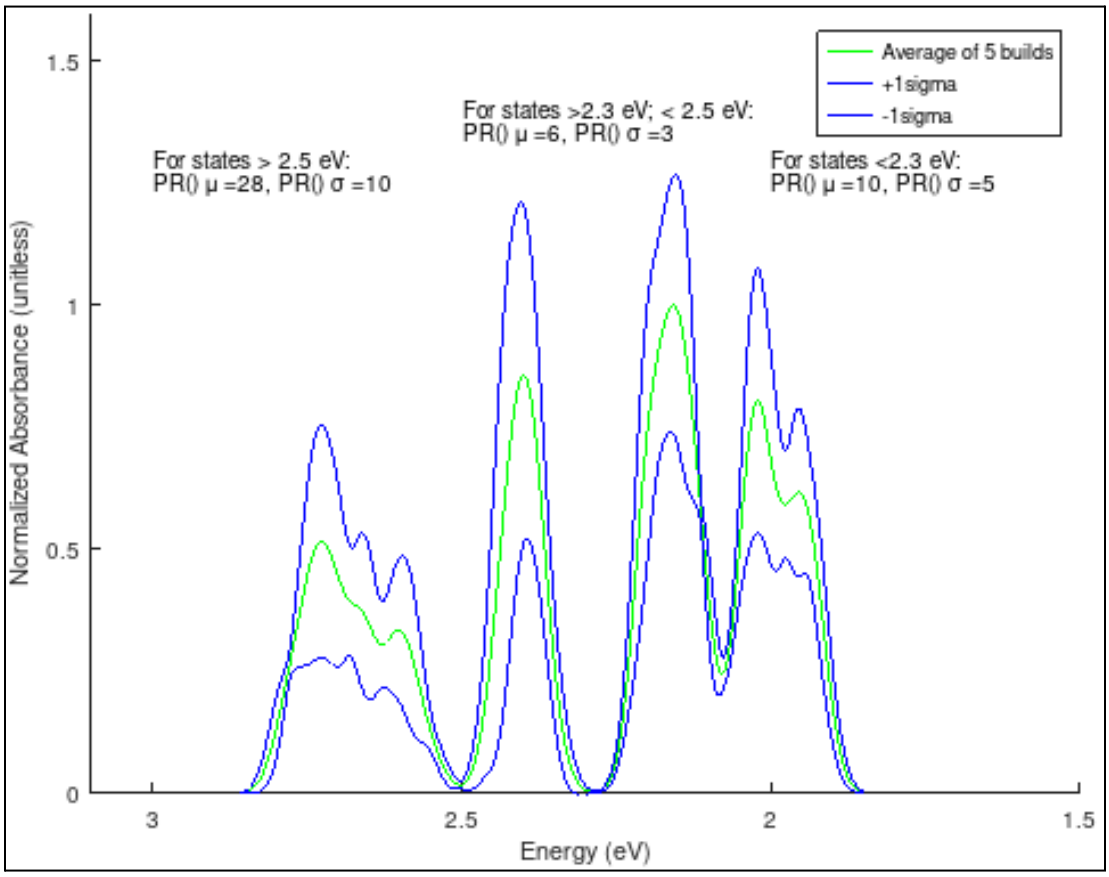

Figure 17d *Averaged absorption spectrum of 5 repeated simulations of a 4x5x5 unit system. The site energy noise has a standard deviation of 0.05 eV and the peak convolution width is set at 0.1 eV. Spectra are normalized by assigning the energy with the largest average absorption a value of 1 and applying this scaling factor to all other absorption values across the energy range. The system eigenenergies greater than 2.5 eV have a PR() average of 28 with a standard deviation of 10. The system eigenenergies between 2.5 and 2.3 eV have a PR()*

average of 6 with a standard deviation of 3. The system eigenenergies less than 2.3 eV have a PR() average of 10 with a standard deviation of 5.

With the larger systems in the pi-stacking dimension the trend continues (Figure 18). The peaks in the predicted spectrum for the larger systems lose resolution at the same convolution width as the spectrum becomes more crowded as more coupled, excited states become available. As with the 3x5x5 unit system, the larger systems gradually have red-shifted absorption peaks with more contribution from delocalized excitons than localized excitons represented by the peak at 2.3 eV. This redshift can be quantified by comparing the excitation energy at the 50% absorption intensity relative to the band edge peak. Between the 3x5x5, 4x5x5, and 9x5x5 unit systems, the band edge half height shifts from 1.95 to 1.9 eV and then to 1.85 eV as the system size increases. This redshifted behavior would be advantageous for commercial application so the PDBD-T-2F sites better match the red-dominant solar spectrum.

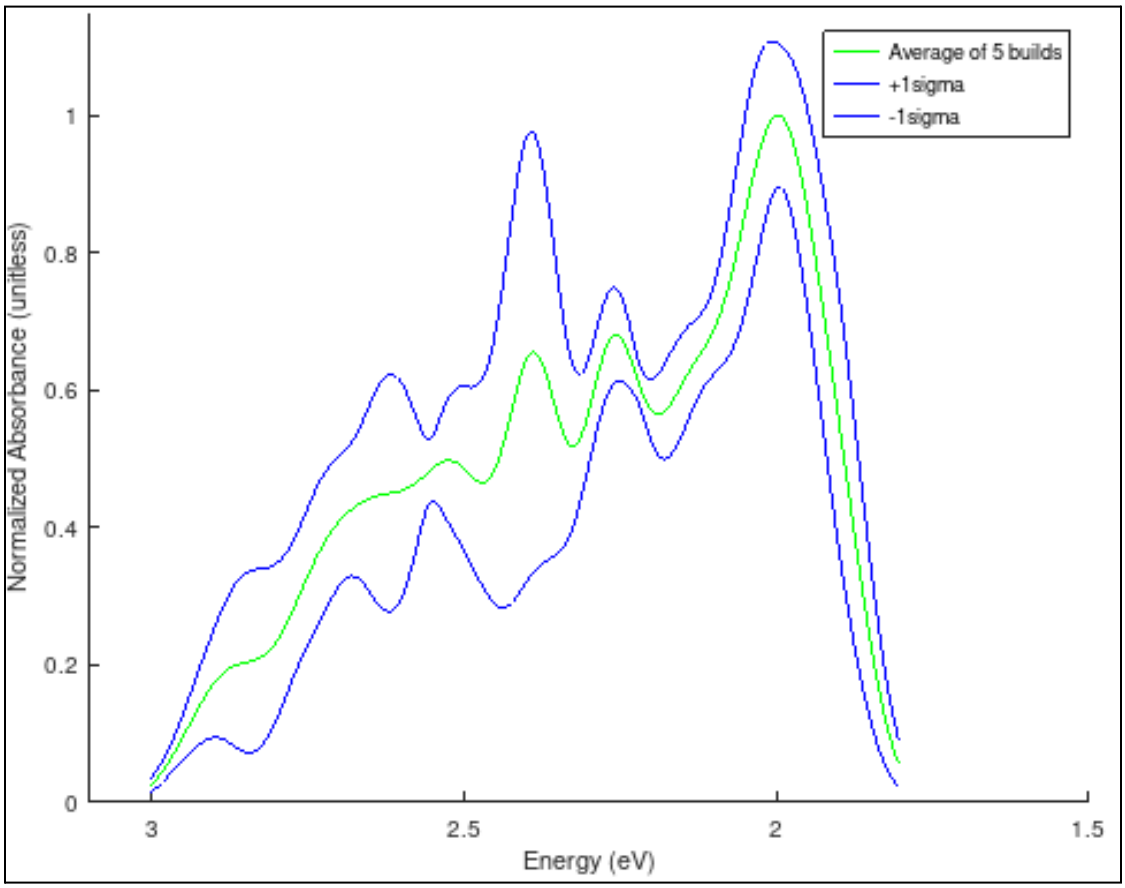

Figure 18 *This larger 9x5x5 unit system exhibits a similar absorption spectrum as the 4x5x5 unit system (Figure 17d) with slight redistribution to red shifted wavelengths. Displayed spectrum is the average of 5 repeated simulations with a site energy noise standard deviation of 0.05 eV and a peak convolution width of 0.1 eV. Spectra are normalized by assigning the energy with the largest average absorption a value of 1 and applying this scaling factor to all other absorption values across the energy range.*

While there are distinct changes to the absorption spectrum between each of the model cases shown in Figure 17, general trends occur for the delocalization character of the systems. To account for each system's different maximum PR() value caused by their different number of sites, the PR() value can be normalized by dividing by the number of sites in the system

(Equation 10b). In a similar vein the relative standard deviation can be used to compare the PR() standard deviations between systems with different average PR() values (Equation 10b)

$$PR()_{normalized} = \frac{PR()}{total\ sites} \quad (10a)$$

$$Relative\ standard\ deviation = \frac{\sigma}{\mu} \quad (10b)$$

The largest changes in $PR()_{normalized}$ occurs between monolayer and bilayer pi-stacked systems increasing from 0.056 to 0.10 for the band edge peak. The 3x5x5 and 4x5x5 unit systems have similar $PR()_{normalized}$ values of 0.11 and 0.10 to that of the bilayer system. These stabilizing trends suggest even larger systems than these studied systems would have similar behavior. The average excitons delocalize across approximately 14% of the monomer sites although the relative standard deviation remains high, above 0.7, indicating there is variability in the extent of delocalization between eigenstates.

At energies greatly above the band edge, the predicted spectrum deviates from the experimental spectrum in part because the model only includes the lowest lying singlet excited state of the constituent monomer. This model design ignores absorption to the higher lying excited states that contribute to the high-energy region of the experimental spectrum. DFT calculation of the monomer predicted higher lying singlet excited states at 2.53, 2.66, and 2.94 eV, which would all alter the simulated absorption spectrum between 2.5 and 3.0 eV if included. For higher energy photons in real systems, additional excited states are accessible and would alter the shape of the absorption spectrum for energies above the PDBD-T-2F monomer first excited state energy (2.3 eV).

3.2 Effects of site energy noise on absorption spectra

Adjusting the magnitude of the pseudo-random site energy noise parameter also impacts the absorption spectrum. With zero site energy noise, the excitation energies are reduced to a select few values as the coupling interactions are equivalent for every equally spaced and

oriented monomer. This creates dense packing of excited states, creating sharp peaks that are mainly broadened by the coupling induced broadening and the convolution width set at 0.05 eV (Figure 19). With increased noise, the absorption spectrum broadens and absorbs more uniformly across the range.

Interpretation of these effects is partially limited because the line dipole coupling calculations do not adjust for varied site energy. In a real system, the forces that adjust the site energy causing variation may also affect the orientation or spacing which would impact the coupling energy between sites.

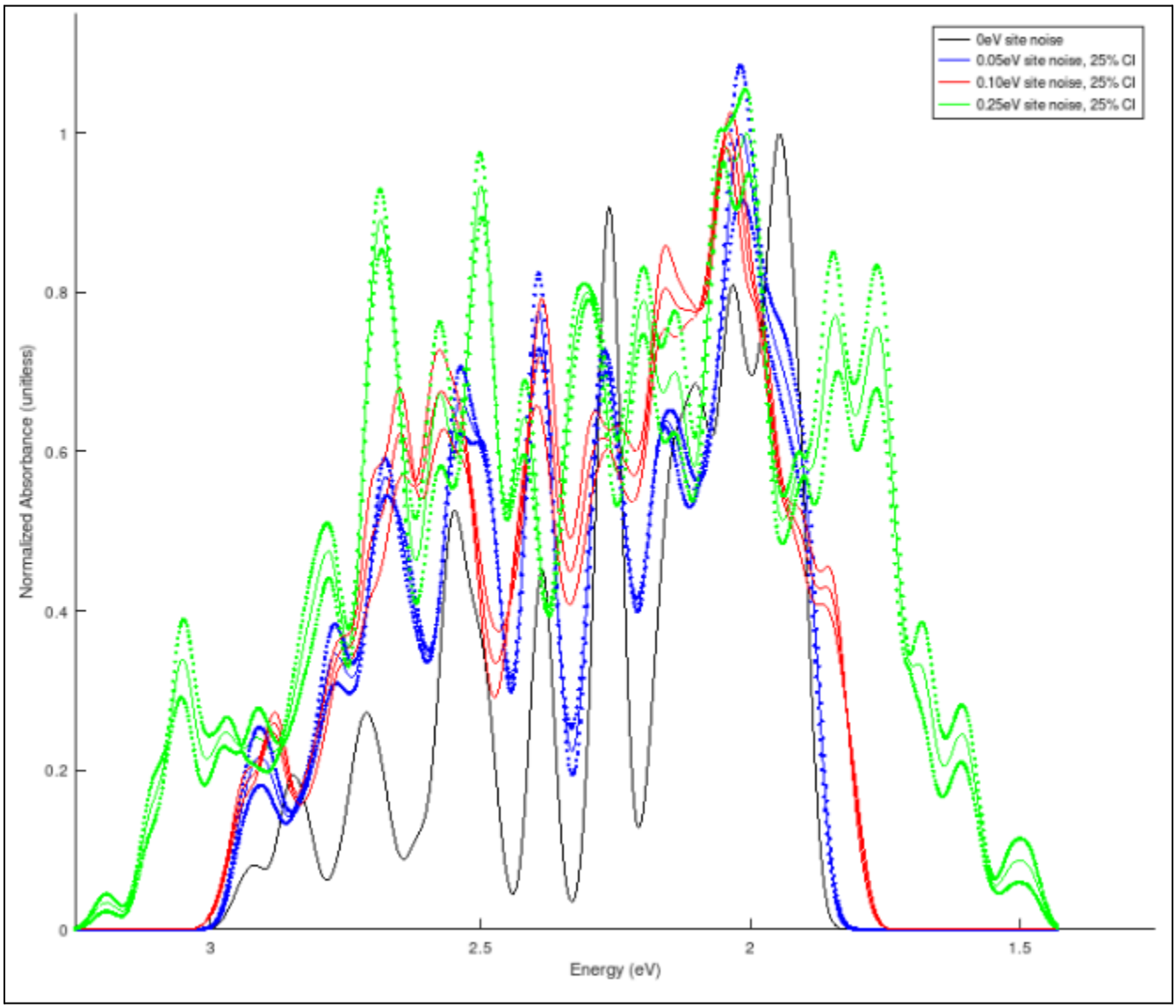

Figure 19 *Increasing site noise widens the absorption spectrum. Displayed spectra are an average from 3 absorption spectra with changing site energy noise standard deviation between each colored spectrum and include their 25% confidence intervals. Site energy noise standard deviation ranges from 0 to 0.25 eV. All spectra use a peak convolution width of 0.05 eV. Spectra are normalized by assigning the energy with the largest average absorption a value of 1 and applying this scaling factor to all other absorption values across the energy range.*

With a site energy of 0.05 eV and a convolution width of 0.25 eV the simulated PDBD-T-2F absorption spectrum has similar band gap energy as the spectrum reported in literature with both occurring at 1.9 eV (Figure 20a). This result suggests the assumptions employed in the model are appropriate for this level of analysis. Additional simulated and empirical data could validate this correlation or narrow the useful scope with this model's approximations.

While it is possible to model 0.25 eV of broadening, this is actually about one order of magnitude greater than the expected temperature-induced broadening at the model's room temperature.[64] The correlation between simulated spectra with larger convolution widths and the experimental spectrum of PDBD-T-2F could indicate that there are additional sources of inconsistency in the experimental crystal. This connection was further investigated by varying the site energy noise parameter as a direct representative of lattice defects or molecule irregularities in the experimental crystal (Figure 20b). The simulated absorption spectrum with an increased site energy of 0.1 eV and a more realistic convolution width of 0.05 eV also showed a similar band edge energy to the reported experimental behavior of PDBD-T-2F.

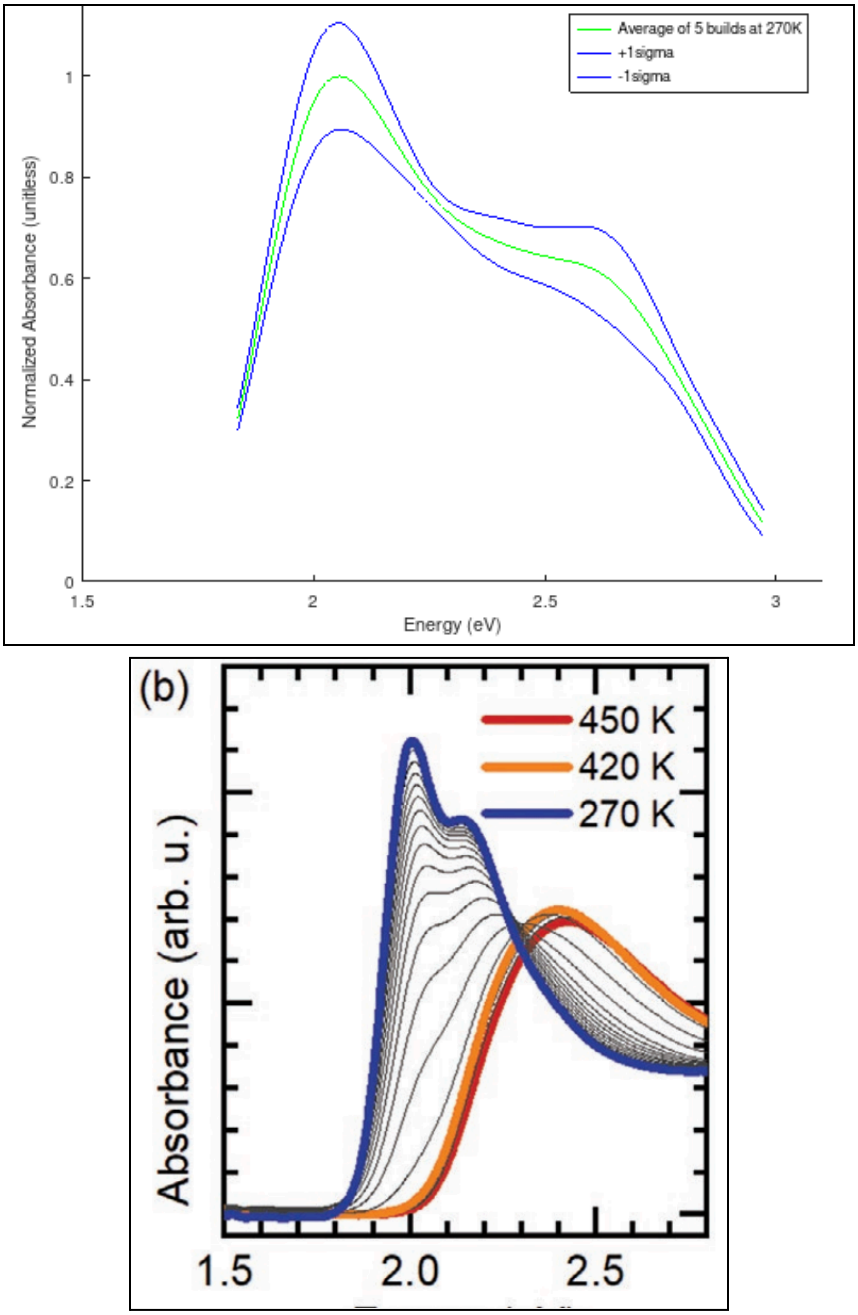

Figure 20a *The modeled spectrum for a PDBD-T-2F system with a convolution width of 0.25 eV (Top) has relatable features to the empirical spectrum reported at 270 K by Kroh et al. (Bottom, Figure 7b).*[62] *Note the energy axis is inverted versus the rest of the simulated spectra presented above. Top panel spectrum is an average of 5 repeated simulations with a site energy noise standard deviation of 0.05 eV. Simulated spectra are normalized by assigning the energy with the largest average absorption a value of 1 and applying this scaling factor to all other absorption values across the energy range.*

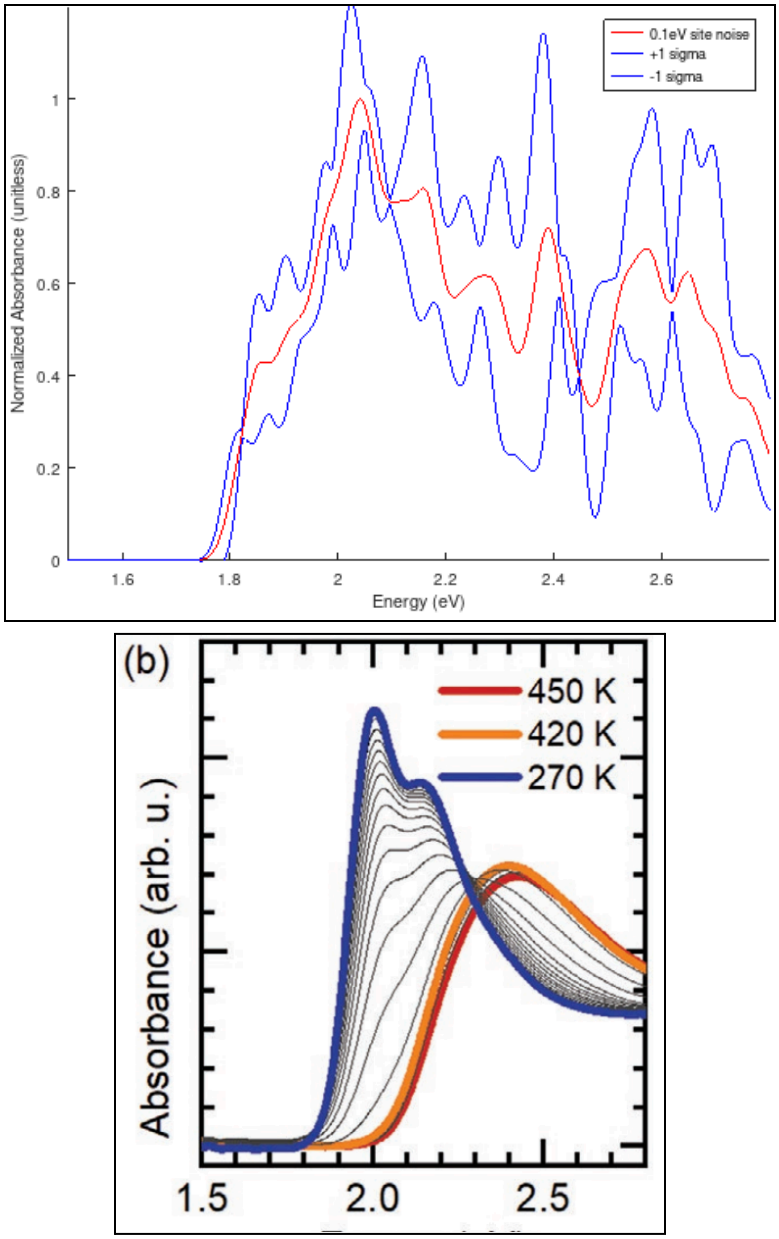

Figure 20b *The modeled spectrum for a PDBD-T-2F system with a realistic convolution width of 0.05 eV for a room temperature system (Top) has relatable features to the empirical spectrum reported at 270 K by Kroh et al. (Bottom, Figure 7b).*[62] *Note the energy axis is inverted versus the rest of the simulated spectra presented above. Top panel spectrum is an average of 3 repeated simulations with a site energy noise standard deviation of 0.1 eV. Simulated spectra are normalized by assigning the energy with the largest average absorption a value of 1 and applying this scaling factor to all other absorption values across the energy range.*

Within the absorption spectra, the delocalization behavior is highly varied between eigenenergies as suggested by the large relative standard deviation of the PR() index for every system geometry. This variation is non-random with distinct behavior for each absorption peak. high-energy peaks have the individual eigenstates with the largest PR() value of 447 as well as the highest average PR() of 171 (Figure 21). The 2.31 eV site energy peak has the lowest average PR() of 18.5 as well as the smallest standard deviation of PR() delocalization at 13.0. Low-energy peaks less than the site energy have moderate PR() values averaging 44.1 with peaks lower in energy having more delocalization than peaks near the site energy. Excitons with larger PR() values are more likely to have some probability at the system edge, which allows exciton harvesting. Understanding the shape of delocalization can inform whether two delocalization patterns with similar PR() values will have similar likelihoods to reach the interface and eventually generate useful power.

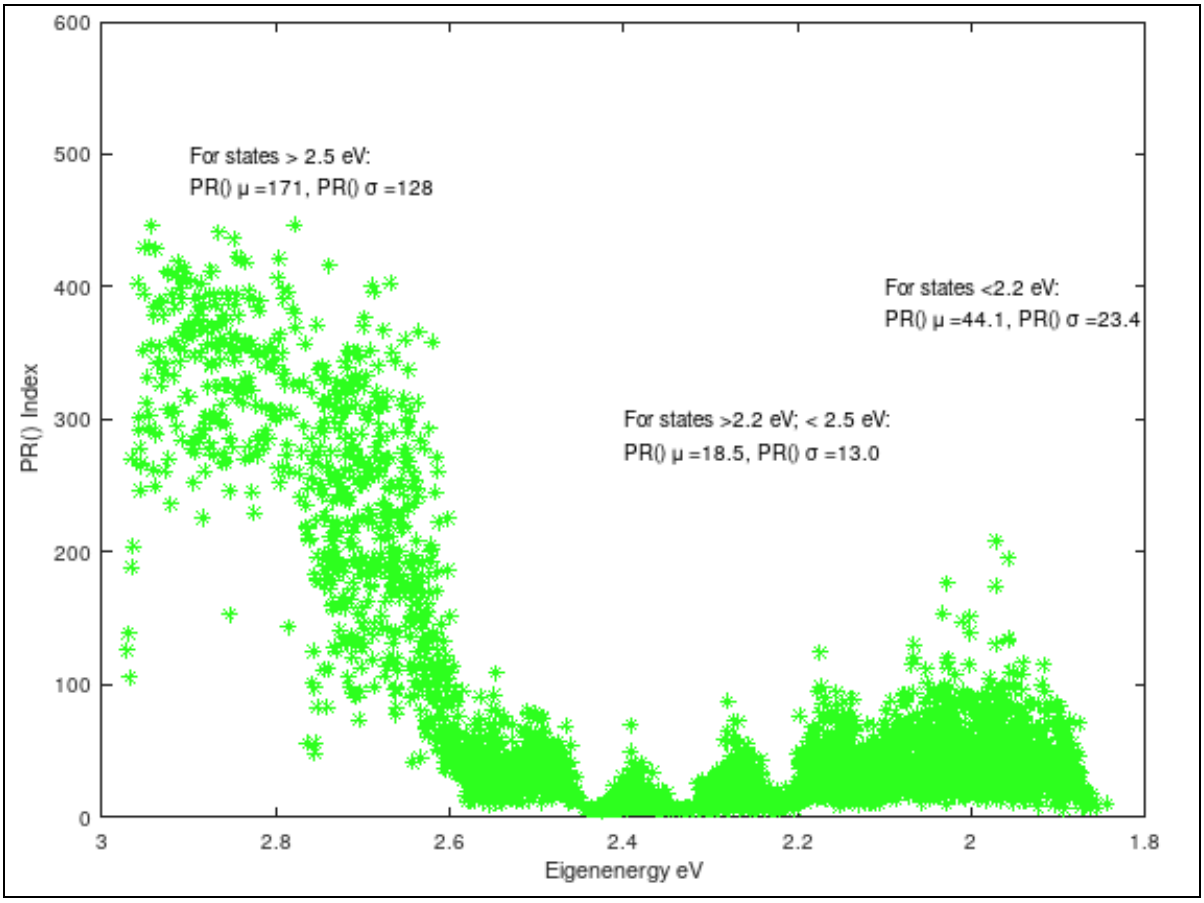

Figure 21 *PR() values from 5 repeated simulations were plotted by eigenenergy for each exciton in a 9x15x9 unit system built with 0.05 eV site noise. Higher energy eigenstates have higher individual and average PR() index values. Lowest relative PR() values occur at the site energy of 2.31 eV. The system eigenenergies greater than 2.5 eV have a PR() average of 171 with a standard deviation of 128. The system eigenenergies between 2.5 and 2.2 eV have a PR() average of 18.5 with a standard deviation of 13. The system eigenenergies less than 2.2 eV have a PR() average of 44.1 with a standard deviation of 23.4.*

For the high-energy regime of the absorption spectrum, a representative 2.9 eV eigenstate with a PR() of 300 is shown as Figure 22a. This eigenstate has two separated areas of high probability. In each of these areas, the probability of site occupancy is roughly equal in the pi-stacking direction with diminishing likelihood of occupancy in the down-chain and

intra-lamellar directions at sites further away from the center of each area. The symmetry between the two areas of high occupancy probability suggest a single node bisecting the intra-lamellar axis creates this probability distribution.

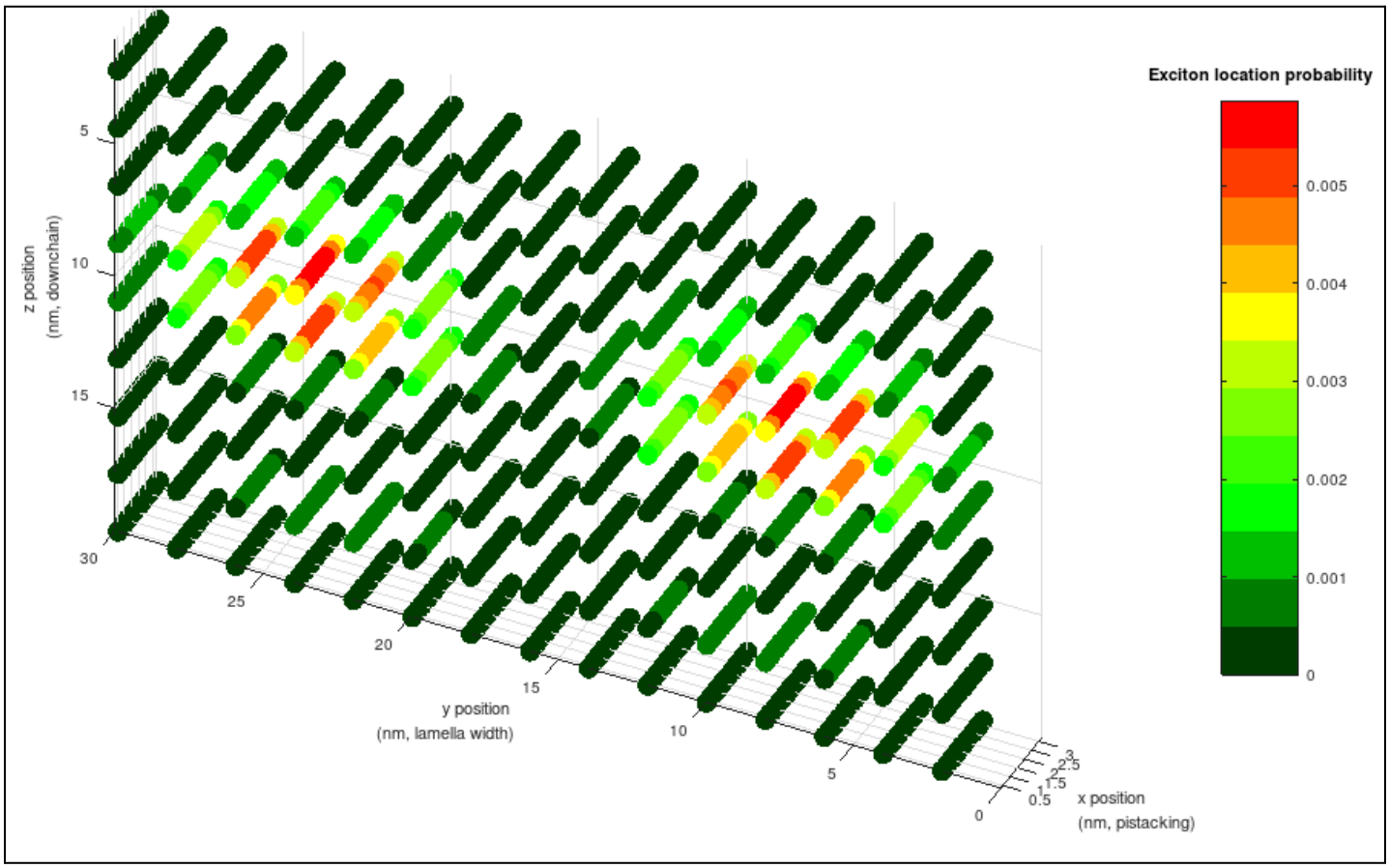

Figure 22a *Visual delocalization for representative exciton of 2.9 eV excitation energy for a 9x15x9 unit system. The exciton has a PR() value of 300. The exciton is delocalized with a bimodal concentration suggesting a node across the intra-lamellar direction.*

In comparison, the 2.3 eV eigenstate in Figure 22b has a PR() value of 9. This state is visually similar to many of the eigenstates around the site excitation energy with the probability of occupancy dispersed throughout the system. For this eigenstate some of the highly likely sites are isolated while others are immediately neighboring another probable site in the down-chain direction. There are no neighboring sites in the intra-lamellar direction which both have a high

likelihood of occupancy. In the pi-stacking dimension all of the potentially occupied sites are toward the edge of the system. This busier representation of the exciton delocalized probability may have multiple nodes in all three directions to create these relatively isolated potentially occupied sites.

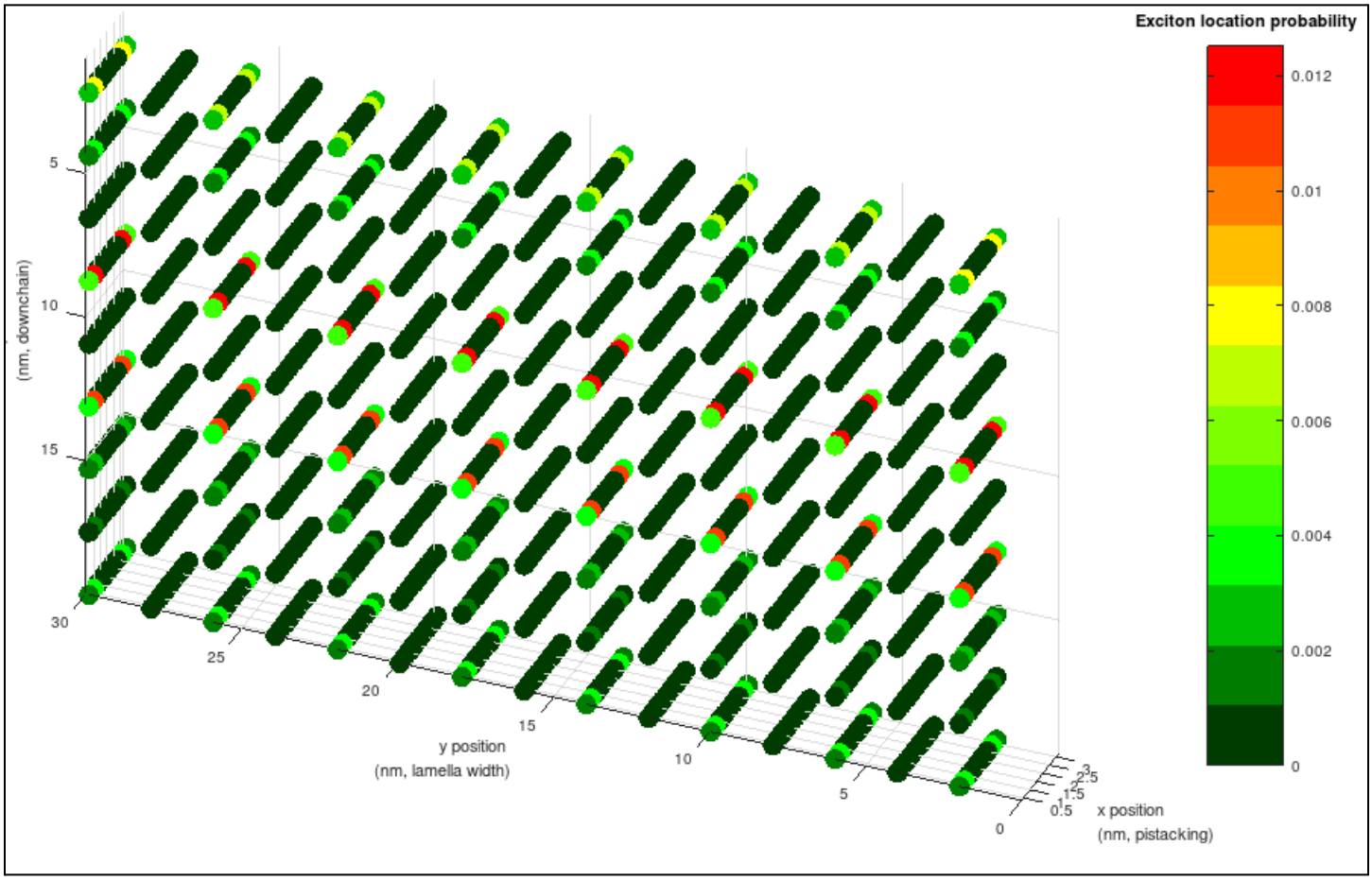

Figure 22b *Visual delocalization for representative exciton of 2.3 eV excitation energy for a 9x15x9 unit system. The exciton has a PR() value of 9. The exciton is delocalized with nodes in all three axes.*

For the band edge of the spectrum, a 1.9 eV eigenstate with a PR() value of 110 highlighted the observed visual trends in the low-energy excitons as shown in Figure 22c. This moderately delocalized eigenstate shares some similarities with both the highly delocalized high-energy band eigenstates and the mostly localized site energy eigenstates. Like the highly delocalized states, for the band edge eigenstate the likelihood of occupancy diminishes

monotonically in the down-chain and intra-lamellar directions away from the sites with the highest likelihood of occupancy. Like the mostly localized states, this band edge eigenstate has minimal continuity of occupancy in the pi-stacking direction. Similar to the site energy eigenstates, there may be a node dividing the system across the pi-stacking dimension, which decreases the likelihood of occupancy for the sites that are close to the node.

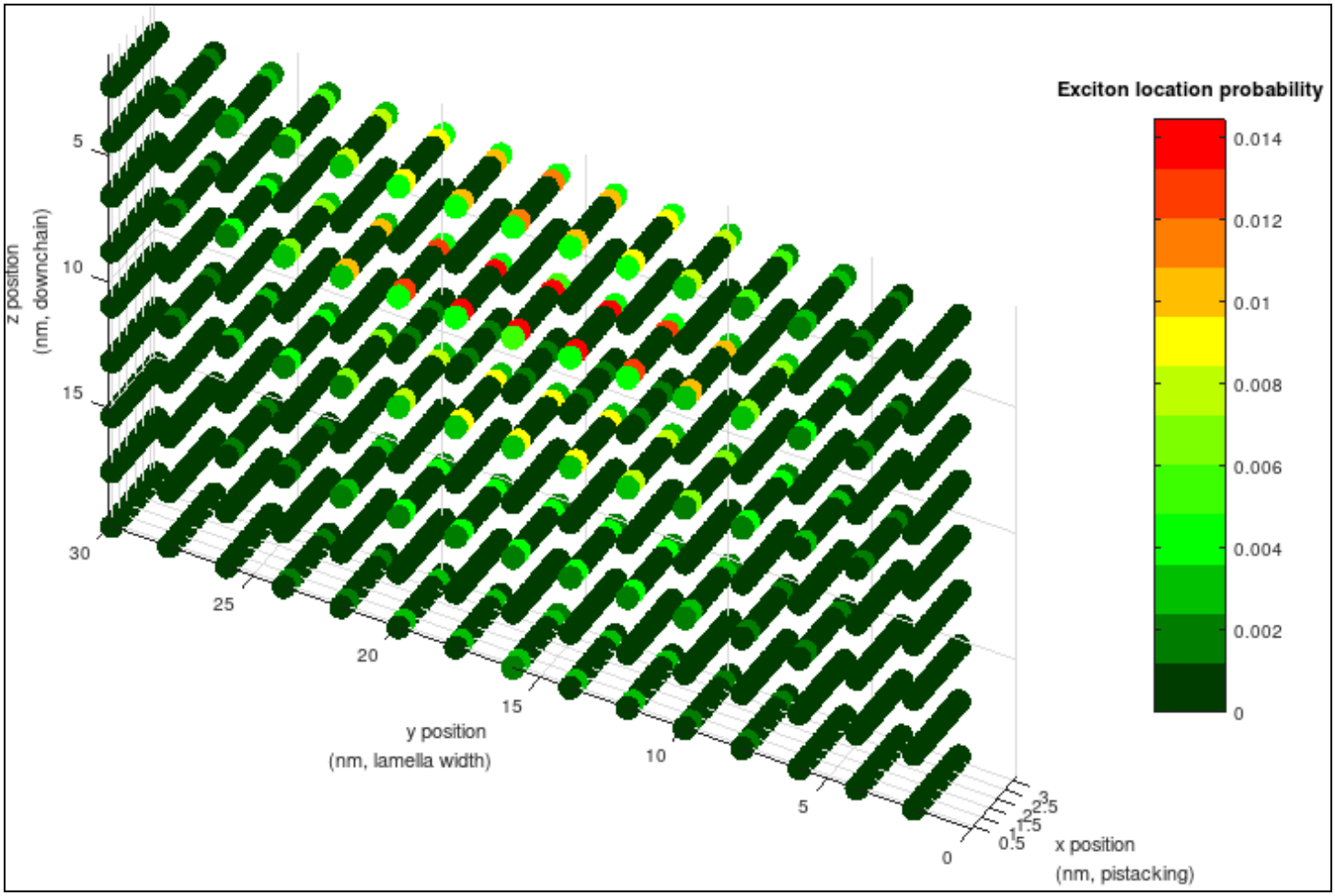

Figure 22c *Visual delocalization for representative exciton of 1.9 eV excitation energy for a 9x15x9 unit system. The exciton has a PR() value of 110. The exciton is asymmetrically delocalized with more probability toward the top face and this probability distribution has nodes in the pi-stacking and down-chain axes.*

3.3 Time propagation effects

When the exciton probability is initially set at one site, the Liouville equation simulates how the population will disperse through time as an ensemble of states. Assigning the entire probability to one site is unphysical in a spectroscopic context because a photon will necessarily produce a delocalized excited state. Nonetheless, the time propagation from a single starting site still simulates the same transport behavior that would be observed in the dynamics of a realistic initial exciton. This means the delocalization behaviors observed from a simplified initial state can be studied as a prediction of the behavior for physically realistic states.

Physically realistic initial states, which are described by the eigenenergies of the initial Hamiltonian, cannot be studied through time in this model because the employed Hamiltonian is time independent. Because the Hamiltonian does not change in time, the initial delocalized states for each excitation energy remain as eigenvectors for the site basis Hamiltonian, which means the site basis population does not move. To bypass this slight limitation of this model would require a time dependent Hamiltonian causing a massive increase in computation time.

The transport behavior was consistent across the tested systems where the initial excited population was localized on one site. Regardless of whether the population was initialized at the center of the system, the edge, or corner, in all cases the exciton population delocalized in the pi-stacking direction with only slight delocalization in the down-chain direction and miniscule delocalization in the intra-lamellar direction.

After 1 fs for a 9x5x5 unit system with the population initially localized on the center monomer, 84% of the population's location probability remains on the center monomer. Of the 16% delocalized location probability, 15% is delocalized to the sites that are pi-stacked with the initial site and less than 1% is delocalized in the down-chain direction (Figure 23a). This very short time simulation demonstrates how the anisotropic transport results are always present and should be expected for physically realistic initial states as well.

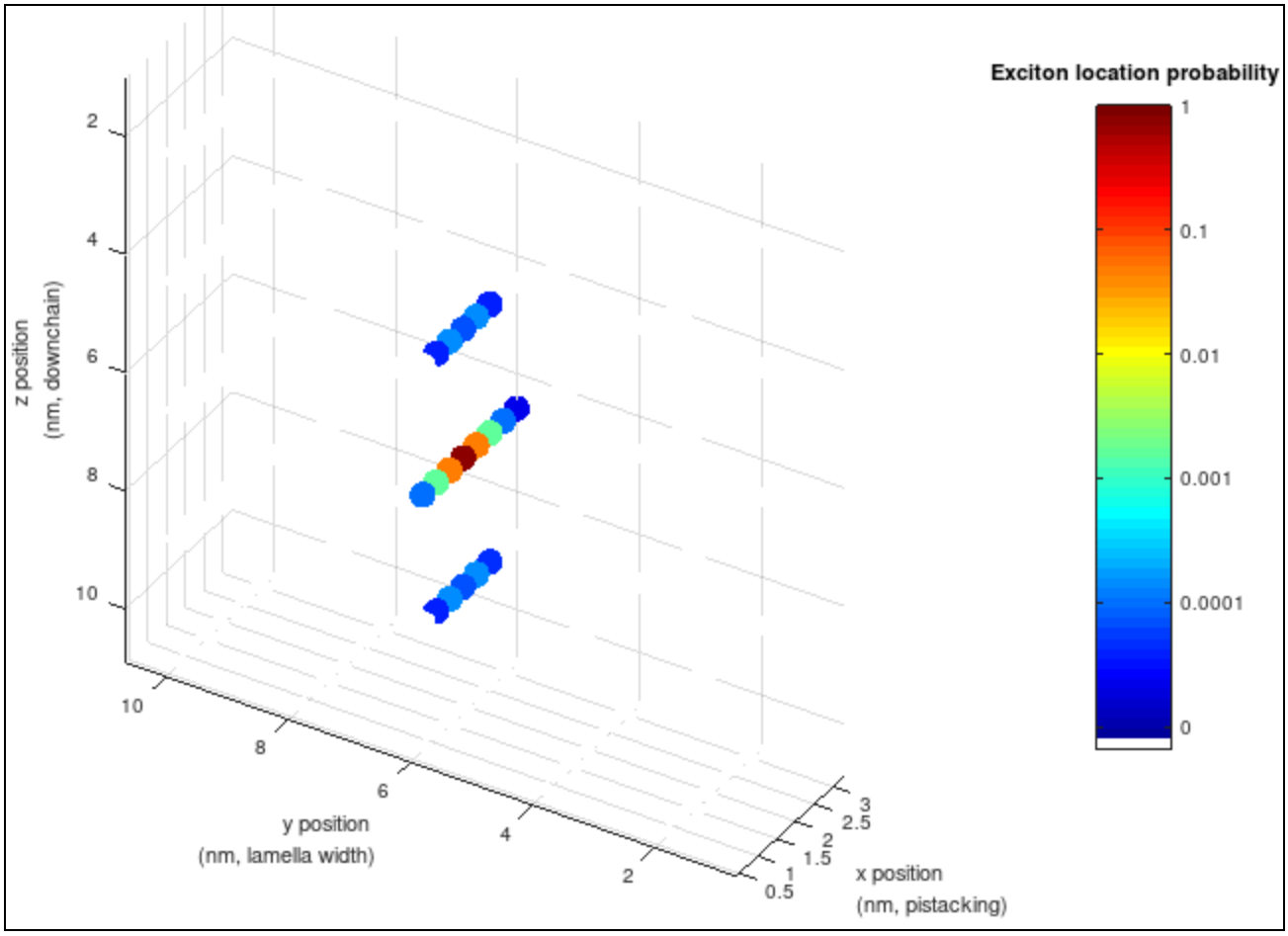

Figure 23a *Delocalization after 1 fs when the exciton population begins localized at the center site of a 9x5x5 unit system. The site energy noise has a standard deviation of 0.05 eV for the single simulation run. Greater than 99% of the population's probability remains constrained to the initial site and the sites that are aligned with the initial site in the pi-stacking direction.*

When the simulation is continued to 10 fs, only 15% of the probability remains at the initial site and 75% of the population probability is delocalized to the pi-stacked sites. Ten percent of the population's probability is delocalized off the initial pi-stacked sites with 7% delocalized to the immediate neighbor sites above or below the pi-stacked sites in the down-chain direction (Figure 23b). Even with the longer simulation time, the majority of the population probability remains constrained to sites aligned in the pi-stacking direction with the initial site.

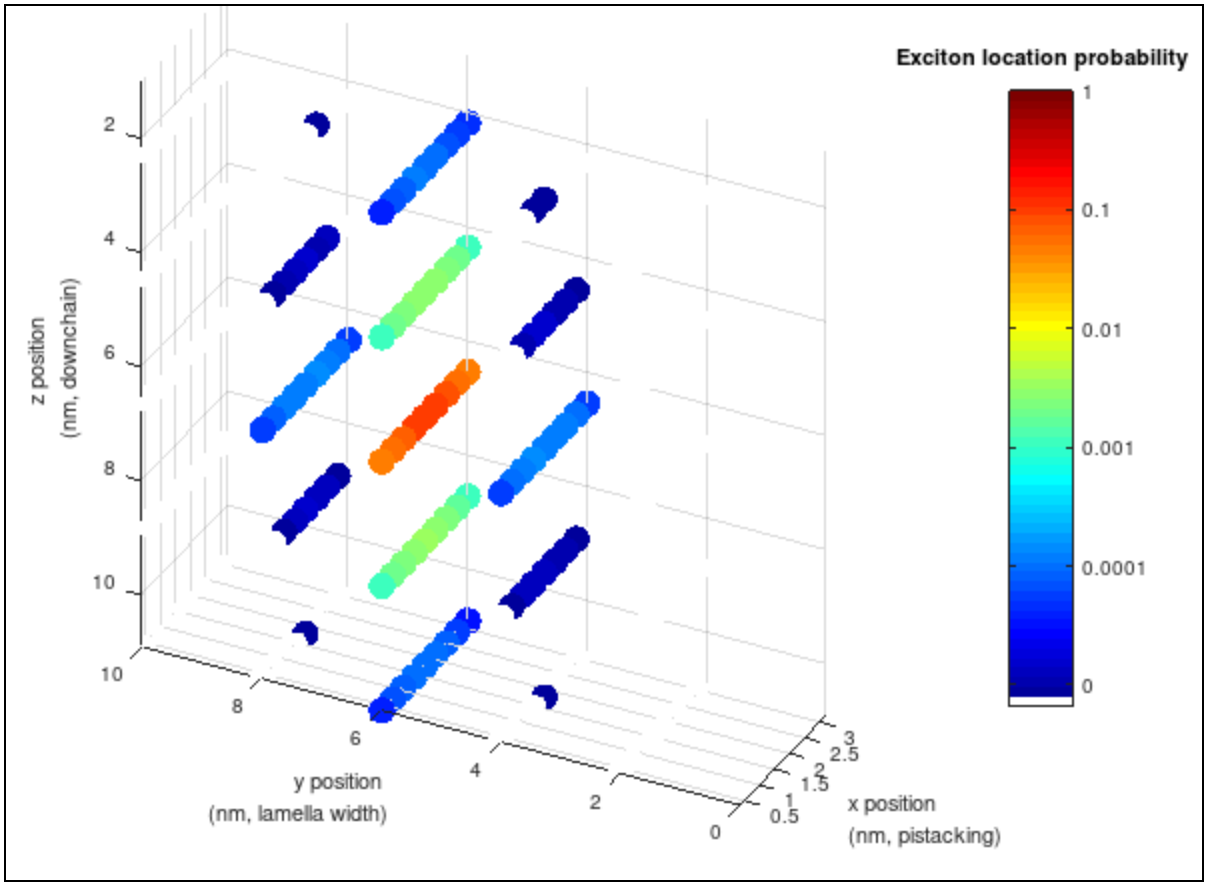

Figure 23b *Delocalization after 10 fs when the exciton population begins localized at the center site of a 9x5x5 unit system. The site energy noise has a standard deviation of 0.05 eV for the single simulation run. The vast majority of the population's probability, 90%, remains constrained to the initial site and the sites that are aligned with the initial site in the pi-stacking direction.*

By 100 fs the quantum delocalization effects are minimal because the dephasing parameter has severely dampened the coupling interactions between sites. The simulation at 100 fs represents a reasonable total delocalization of the exciton population this model predicts due to quantum effects. At 100 fs, 5% of the probability remains on the initial site with 36% of the probability dispersed across the sites in the pi-stacking direction of the initial site. Another 34% of the population's probability is spread in the down-chain direction across the neighboring sites above and below the initial site's pi-stacking direction. The remaining 25% of the exciton's

location probability is spread across the further sites in the down-chain and intra-lamellar directions (Figure 23c). These results suggest that exciton transport occurs primarily down the pi-stacking direction for PDBD-T-2F with a slight change to transport in the down-chain direction, albeit at a much slower rate.

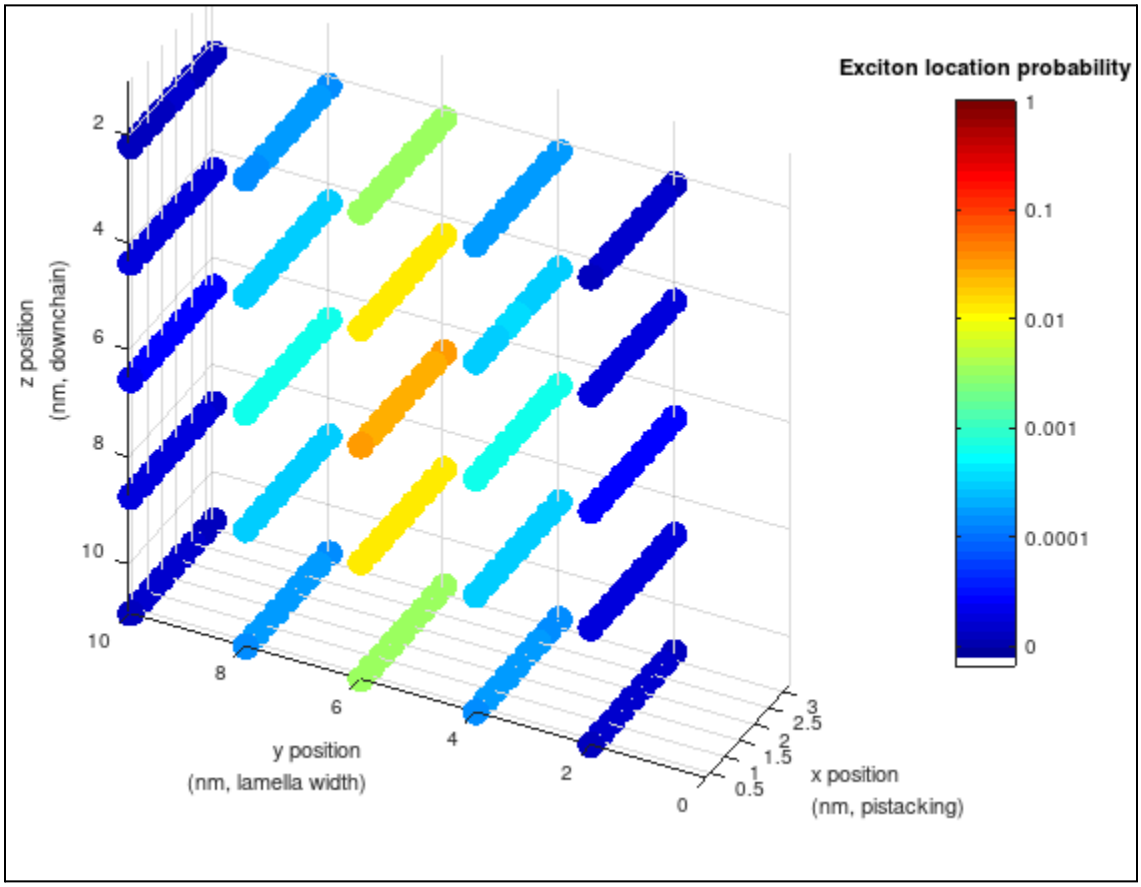

Figure 23c *Delocalization after 100 fs when the exciton population begins localized at the center site of a 9x5x5 unit system. The site energy noise has a standard deviation of 0.05 eV for the single simulation run. Only 41% of the population's probability remains constrained to the initial site and the sites that are aligned with the initial site in the pi-stacking direction.*

To test the propagation limit in the pi-stacking direction, additional systems were simulated with longer crystal lengths in the pi-stacking direction. While this longer system is not presently reported in laboratory created crystals, it is useful to predict how far an exciton can

travel by way of quantum delocalization within 100 fs. To test this question, a 20x3x3 unit system was simulated with the exciton initially starting localized at the center of the edge lamella. After 100 fs the exciton delocalized predominantly down the pi-stacking chain with more than half (55%) of the probability constrained to the first 7 pi-stacking lamellar sheets (Figure 24).

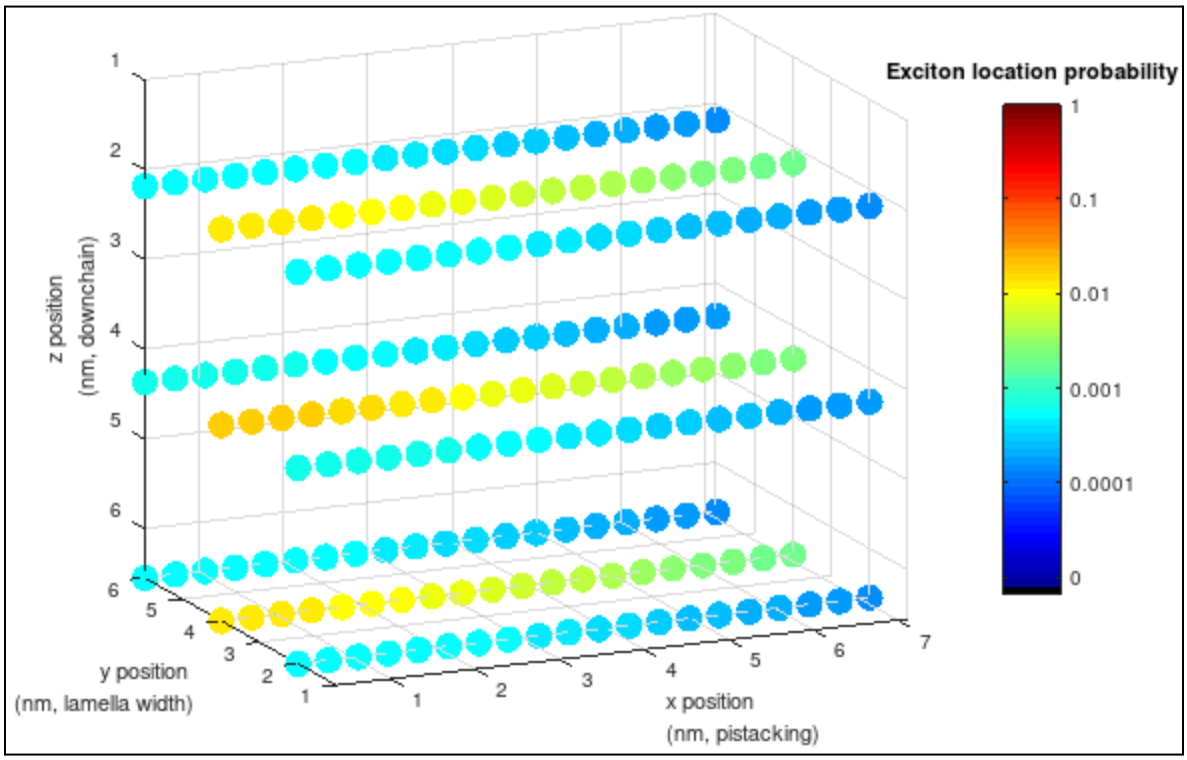

Figure 24 *Delocalization after 100 fs when the exciton population begins localized on the left edge lamella for a 20x3x3 unit system. The site energy noise has a standard deviation of 0.05 eV for the single simulation run.*

The minimal distance the exciton travels in the pi-stacking direction helps to bound the useful crystal size for future PDBD-T-2F devices. Once a crystal is larger than 14 pi-stacking sites (4.98 nm), it is expected that the quantum transport contribution to the power conversion efficiency would be severely lowered as centralized fractions of the initial exciton's probability could not delocalize to the domain boundary before dephasing stops coherent transport. Quantum

transport is not the only mechanism to move excitons toward domain boundaries enabling charge separation; Förster hopping describes exciton transport at slower, non-ultrafast timescales.[27]

Modeling helps discern which transport mechanisms drive experimental performance. Lee *et al.* report exciton diffusion lengths in PDBD-T-2F bilayer heterojunctions ranging from 11.3 to 15.3 nm with power conversion efficiencies between 9 and 10%.[65] Lee *et al.*'s diffusion range falls within the larger range reported for similar OPV devices which may have diffusion lengths between 5 and 45 nm.[24,34]

As the maximum power conversion efficiency for isolated PDBD-T-2F is 17% per the Shockley-Queisser limit, about 59% of the exciton population's probability would need to achieve charge transfer to meet Lee *et al.*'s reported 10% efficiency. This simulation predicts quantum delocalization could transport 59% of the exciton population's probability across 5 pi-stacking lamellar sheets (1.78 nm) before decoherence inhibits quantum behavior. Because twice distance, accounting for symmetric travel in both pi-stacking directions, is substantially lower than the reported diffusion lengths, it is likely that the PDBD-T-2F system also relies on Förster hopping exciton movement to achieve its reported power conversion efficiency. This reliance on both some quantum delocalization and some classical hopping means that mechanisms that lower either method of transport could lower the PDBD-T-2F system performances.

Section 4: Conclusion

The line-dipole method is an improvement over the point dipole method by increasing the model accuracy when calculating coupling for closely packed sites. Supplemented with DFT coupling calculations for the closest interactions, the line dipole method enables quick modeling of full size domains for a PDBD-T-2F system without requiring supercomputing resources.

The simulations from this model elucidate the effect pi-stacking interactions have on the predicted absorption spectra. Adjustments to the site noise demonstrated that the simulated spectra from this model are in general agreement with the band edge for experimental PDBD-T-2F systems. The corresponding eigenenergies of the absorption spectrum have specific delocalization patterns with minimal delocalization of states around the site energy and moderate delocalization for low-energy states at the band edge. The model's site basis enabled study of the system dynamics to predict how site occupancy probability changes over time. The resultant anisotropic delocalization preferentially spread along the pi-stacking direction with slight delocalization in the down-chain direction as well. Within the many femtosecond timescale where quantum transport effects are substantial, the model predicts exciton probability can substantially delocalize across 4.98 nm in the pi-stacking dimension. This delocalization distance is less than the reported exciton diffusion distances reported for PDBD-T-2F systems, which suggests a combination of quantum transport and Förster hopping governs whether an exciton will reach a material interface for harvesting before loss mechanisms stop the travel. In total the model serves as a useful tool to study exciton behavior in polymer systems aiding future development of efficient OPV designs.

Section 5: References

(1) Nabben, D.; Kuttruff, J.; Stolz, L.; Ryabov, A.; Baum, P. Attosecond electron microscopy of sub-cycle optical dynamics. Nature **2023**. DOI: 10.1038/s41586-023-06074-9.

(2) Hsu, C.-P. The Electronic Couplings in Electron Transfer and Excitation Energy Transfer. *Accounts of Chemical Research* **2009**, *42* (4), 509-518. DOI: 10.1021/ar800153f.

(3) Kleinschmidt, A. T.; Chen, A. X.; Pascal, T. A.; Lipomi, D. J. Computational Modeling of Molecular Mechanics for the Experimentally Inclined. *Chemistry of Materials* **2022**, *34* (17), 7620-7634. DOI: 10.1021/acs.chemmater.2c00292.

(4) Melko, R. Machine Learning and the Complexity of Quantum Simulation. Kavli Foundation Special Symposium, 2021.

(5) Simm, G. N.; Proppe, J.; Reiher, M. Error Assessment of Computational Models in Chemistry. *CHIMIA* **2017**, *71* (4), 202. DOI: 10.2533/chimia.2017.202.

(6) Denis; Jean-Christophe. Modelling Ultrafast Exciton Transfer in Fluorene-Based Organic Semiconductors. Heriot Watt University, 2013.

(7) Kim, E. C.; Na, S.-I.; Park, J. T. Fogging, reflection, and dust-free transparent conducting glasses based on superhydrophilic nanotextures for organic photovoltaics. *Journal of industrial and engineering chemistry* **2017**, *52*, 243-250.

(8) Burkhard, G.; Hoke, E.; McGehee, M. Accounting for Interference, Scattering, and Electrode absorption to Make Accurate Internal Quantum Efficiency Measurements in Organic and Other Thin Solar Cells. Wiley: Advanced Materials, 2010; Vol. 22, p 4.

(9) de la Perrelle, J. M.; Dolan, A.; Milsom, E. R.; Small, T. D.; Metha, G. F.; Pan, X.; Andersson, M. R.; Huang, D. M.; Kee, T. W. Red-Light-Mediated Photocatalytic Hydrogen Evolution by Hole Transfer from Non-Fullerene Acceptor Y6. *The Journal of Physical Chemistry C* **2022**, *126* (34), 14518-14528. DOI: 10.1021/acs.jpcc.2c05268.

(10) Anikeeva, P.; Beach, G.; Holten-Andersen, N. Electronic, Optical And Magnetic Properties of Materials. MIT, 2013.

(11) Pettersson, L.; Roman, L.; Inganas, O. Modeling photocurrent action spectra of photovoltaic devices based on organic thin films. American Institute of Physics: Journal of Applied Physics, 1999; Vol. 86, p 9.

(12) Nyman, M.; Sandberg, O.; Li, W.; Zeiske, S.; Kerremans, R.; Meredith, P.; Armin, A. Requirements for Making Thick Junctions of Organic Solar Cells based on Nonfullerene Acceptors. Wiley: Solar RRL, 2021; Vol. 5, p 10.

(13) Yu, C.; Gross, P.; Ramakrishna, V.; Rabitz, H.; Mease, K. Selective excitation of molecular eigenstates using state-dependent optical field design. *Chemical Physics Letters* **1996**, *252* (5), 447-456. DOI: https://doi.org/10.1016/0009-2614(96)00200-X.

(14) Zhu, L.; Zhang, M.; Zhong, W.; Leng, S.; Zhou, G.; Zou, Y.; Su, X.; Ding, H.; Gu, P.; Liu, F.; et al. Progress and prospects of the morphology of non-fullerene acceptor based high-efficiency organic solar cells. *Energy & Environmental Science* **2021**, *14* (8), 4341-4357 DOI: 10.1039/D1EE01220G.

(15) Guo, Q.; Guo, Q.; Geng, Y.; Tang, A.; Zhang, M.; Du, M.; Sun, X.; Zhou, E. Recent advances in PM6:Y6-based organic solar cells. *Materials Chemistry Frontiers* **2021**, *5* (8), 3257-3280 DOI: 10.1039/D1QM00060H.

(16) Haase, F.; Hollemann, C.; Schäfer, S.; Merkle, A.; Rienäcker, M.; Krügener, J.; Brendel, R.; Peibst, R. Laser contact openings for local poly-Si-metal contacts enabling 26.1%-efficient

POLO-IBC solar cells. *Solar Energy Materials and Solar Cells* **2018**, *186*, 184-193. DOI: https://doi.org/10.1016/j.solmat.2018.06.020.

(17) Rühle, S. Tabulated values of the Shockley–Queisser limit for single junction solar cells. *Solar Energy* **2016**, *130*, 139-147. DOI: https://doi.org/10.1016/j.solener.2016.02.015.

(18) Zhang, C.; Zhang, Y.; Wang, Z.; Su, Y.; Wei, Z.; Hou, J.; He, S.; Wu, K.; He, C.; Zhang, J.; et al. Probing molecular orientation at bulk heterojunctions by polarization-selective transient absorption spectroscopy. *Science China Chemistry* **2021**, *64* (9), 1569-1576. DOI: 10.1007/s11426-021-1046-6.

(19) Fischer, F. S. U.; Trefz, D.; Back, J.; Kayunkid, N.; Tornow, B.; Albrecht, S.; Yager, K. G.; Singh, G.; Karim, A.; Neher, D. Highly Crystalline Films of PCPDTBT with Branched Side Chains by Solvent Vapor Crystallization: Influence on Opto‐Electronic Properties. *Advanced materials* **2015**, *27* (7), 1223-1228.

(20) Kupgan, G.; Chen, X. K.; Brédas, J. L. Molecular packing of non-fullerene acceptors for organic solar cells: Distinctive local morphology in Y6 vs. ITIC derivatives. *Materials Today Advances* **2021**, *11*, 100154. DOI: https://doi.org/10.1016/j.mtadv.2021.100154.

(21) Armin, A.; Jansen-van Vuuren, R. D.; Kopidakis, N.; Burn, P. L.; Meredith, P. Narrowband light detection via internal quantum efficiency manipulation of organic photodiodes. *Nature Communications* **2015**, *6* (1), 6343. DOI: 10.1038/ncomms7343.

(22) Yuan, X.; Zhao, Y.; Zhan, T.; Oh, J.; Zhou, J.; Li, J.; Wang, X.; Wang, Z.; Pang, S.; Cai, P.; et al. A donor polymer based on 3-cyanothiophene with superior batch-to-batch reproducibility for high-efficiency organic solar cells. *Energy & Environmental Science* **2021**, *14* (10), 5530-5540, 10.1039/D1EE01957K.

(23) Liu, Q.; Fang, J.; Wu, J.; Zhe, L.; Guo, X.; Liu, F.; Zhang, M. Tuning Aggregation Behavior of Polymer Donor via Molecular-Weight Control for

(24) Achieving 17.1% Efficiency Inverted Polymer Solar Cells. Chinese Journal of Chemistry, 2021; Vol. 39, pp 1941-1947.

(25) Janke, S. M.; Qarai, M. B.; Blum, V.; Spano, F. C. Frenkel–Holstein Hamiltonian applied to absorption spectra of quaterthiophene-based 2D hybrid organic–inorganic perovskites. *The Journal of Chemical Physics* **2020**, *152* (14), 144702. DOI: 10.1063/1.5139044.

(26) Clarke, T. M.; Durrant, J. R. Charge Photogeneration in Organic Solar Cells. *Chemical Reviews* **2010**, *110* (11), 6736-6767. DOI: 10.1021/cr900271s.

(27) Dimitriev, O. P. Dynamics of Excitons in Conjugated Molecules and Organic Semiconductor Systems. *Chemical Reviews* **2022**, *122* (9), 8487-8593. DOI: 10.1021/acs.chemrev.1c00648.

(28) Orgil, K. Comparison of Organic and Inorganic Solar Photovoltaic Systems. California Polytechnic State University, 2018.

(29) Gueymard, C. SMARTS, A Simple Model of the Atmospheric Radiative Transfer of Sunshine: Algorithms and Performance Assessment. In *Professional Paper FSEC-PF-270-95*, Florida Solar Energy Center, 1995.

(30) Gueymard, C. Parameterized Transmittance Model for Direct Beam and Circumsolar Spectral Irradiance. *Solar Energy* **2001**, *71* (5), 325-346.

(31) Liu, Y.; Zojer, K.; Lassen, B.; Kjelstrup-Hansen, J.; Rubahn, H.-G.; Madsen, M. Role of the Charge-Transfer State in Reduced Langevin Recombination in Organic Solar Cells: A Theoretical Study. *The Journal of Physical Chemistry C* **2015**, *119* (47), 26588-26597. DOI: 10.1021/acs.jpcc.5b08936.

(32) Lanzani, G. *The Photophysics behind Photovoltaics and Photonics*; John Wiley & Sons, 2012.

(33) Grüne, J.; Londi, G.; Gillett, A. J.; Stähly, B.; Lulei, S.; Kotova, M.; Olivier, Y.; Dyakonov, V.; Sperlich, A. Triplet Excitons and Associated Efficiency-Limiting Pathways in Organic Solar Cell Blends Based on (Non-) Halogenated PBDB-T and Y-Series. *Advanced Functional Materials* **2023**, *33* (12), 2212640. DOI: https://doi.org/10.1002/adfm.202212640.

(34) Peng, Z.; Ye, L.; Ade, H. Understanding, quantifying, and controlling the molecular ordering of semiconducting polymers: from novices to experts and amorphous to perfect crystals. *Materials Horizons* **2022**, *9* (2), 577-606, 10.1039/D0MH00837K.

(35) Firdaus, Y.; Le Corre, V. M.; Karuthedath, S.; Liu, W.; Markina, A.; Huang, W.; Chattopadhyay, S.; Nahid, M. M.; Nugraha, M. I.; Lin, Y.; et al. Long-range exciton diffusion in molecular non-fullerene acceptors. *Nature Communications* **2020**, *11* (1), 5220. DOI: 10.1038/s41467-020-19029-9.

(36) Popp, W.; Brey, D.; Binder, R.; Burghardt, I. Quantum Dynamics of Exciton Transport and Dissociation in Multichromophoric Systems. *Annual Review of Physical Chemistry* **2021**, *72* (1), 591-616. DOI: 10.1146/annurev-physchem-090419-040306.

(37) Pullerits, T.; Freiberg, A. Kinetic model of primary energy transfer and trapping in photosynthetic membranes. *Biophysical Journal* **1992**, *63* (4), 879-896. DOI: https://doi.org/10.1016/S0006-3495(92)81688-0.

(38) Fratini, S.; Mayou, D.; Ciuchi, S. The Transient Localization Scenario for Charge Transport in Crystalline Organic Materials. *Advanced Functional Materials* **2016**, *26* (14), 2292-2315. DOI: https://doi.org/10.1002/adfm.201502386.

(39) You, Z.-Q.; Hsu, C.-P. Theory and calculation for the electronic coupling in excitation energy transfer. *International Journal of Quantum Chemistry* **2014**, *114* (2), 102-115. DOI: https://doi.org/10.1002/qua.24528.

(40) Barford, W. Exciton transfer integrals between polymer chains. *Journal of chemical physics.* **2007**, *126* (13), 134905. DOI: 10.1063/1.2714516.

(41) Beenken, W. J.; Pullerits, T. Excitonic coupling in polythiophenes: Comparison of different calculation methods. *The Journal of chemical physics* **2004**, *120* (5), 2490-2495.

(42) Grage, M. M. L.; Zaushitsyn, Y.; Yartsev, A.; Chachisvilis, M.; Sundström, V.; Pullerits, T. Ultrafast excitation transfer and trapping in a thin polymer film. *Physical review.* **2003**, *67* (20), 205207. DOI: 10.1103/PhysRevB.67.205207.

(43) Gaussian 16, Revision A.03, M. J. Frisch, G. W. Trucks, H. B. Schlegel, G. E. Scuseria, M. A. Robb, J. R. Cheeseman, G. Scalmani, V. Barone, G. A. Petersson, H. Nakatsuji, X. Li, M. Caricato, A. Marenich, J. Bloino, B. G. Janesko, R. Gomperts, B. Mennucci, H. P. Hratchian, J. V. Ortiz, A. F. Izmaylov, J. L. Sonnenberg, D. Williams-Young, F. Ding, F. Lipparini, F. Egidi, J. Goings, B. Peng, A. Petrone, T. Henderson, D. Ranasinghe, V. G. Zakrzewski, J. Gao, N. Rega, G. Zheng, W. Liang, M. Hada, M. Ehara, K. Toyota, R. Fukuda, J. Hasegawa, M. Ishida, T. Nakajima, Y. Honda, O. Kitao, H. Nakai, T. Vreven, K. Throssell, J. A. Montgomery, Jr., J. E. Peralta, F. Ogliaro, M. Bearpark, J. J. Heyd, E. Brothers, K. N. Kudin, V. N. Staroverov, T. Keith, R. Kobayashi, J. Normand, K. Raghavachari, A. Rendell, J. C. Burant, S. S. Iyengar, J. Tomasi, M. Cossi, J. M. Millam, M. Klene, C. Adamo, R. Cammi, J. W. Ochterski, R. L. Martin, K. Morokuma, O. Farkas, J. B. Foresman, and D. J. Fox, Gaussian, Inc., Wallingford CT, **2016**.

(44) He, Q.; Sheng, W.; Zhang, M.; Xu, G.; Zhu, P.; Zhang, H.; Yao, Z.; Gao, F.; Liu, F.; Liao, X.; et al. Revealing Morphology Evolution in Highly Efficient Bulk Heterojunction and Pseudo-Planar Heterojunction Solar Cells by Additives Treatment. *Advanced Energy Materials* **2021**, *11* (7), 2003390, https://doi.org/10.1002/aenm.202003390.

(45) Hexemer, A.; Muller-Buschbaum, P. Advanced grazing-incidence techniques for modern soft-matter materials analysis. *IUCrJ* **2015**, *2* (1), 106-125.

(46) Mahmood, A.; Wang, J.-L. A Review of Grazing Incidence Small- and Wide-Angle X-Ray Scattering Techniques for Exploring the Film Morphology of Organic Solar Cells. *Solar RRL* **2020**, *4* (10), 2000337, https://doi.org/10.1002/solr.202000337.

(47) Scharsich, C.; Fischer, F. S. U.; Wilma, K.; Hildner, R.; Ludwigs, S.; Köhler, A. Revealing structure formation in PCPDTBT by optical spectroscopy. *Journal of Polymer Science Part B: Polymer Physics* **2015**, *53* (20), 1416-1430, https://doi.org/10.1002/polb.23780.

(48) Brinkmann, M. Directional Epitaxial Crystallization and Tentative Crystal Structure of Poly(9,9‘-di-n-octyl-2,7-fluorene). *Macromolecules* **2007**, *40* (21), 7532-7541. DOI: 10.1021/ma071390d.

(49) Fischer, F. S. U.; Kayunkid, N.; Trefz, D.; Ludwigs, S.; Brinkmann, M. Structural Models of Poly(cyclopentadithiophene-alt-benzothiadiazole) with Branched Side Chains: Impact of a Single Fluorine Atom on the Crystal Structure and Polymorphism of a Conjugated Polymer. *Macromolecules* **2015**, *48* (12), 3974-3982. DOI: 10.1021/acs.macromol.5b00839.

(50) Marina, S.; Gutierrez-Fernandez, E.; Gutierrez, J.; Gobbi, M.; Ramos, N.; Solano, E.; Rech, J.; You, W.; Hueso, L.; Tercjak, A.; et al. Semi-paracrystallinity in semi-conducting polymers. *Materials Horizons* **2022**, *9* (4), 1196-1206, 10.1039/D1MH01349A.

(51) Köntges, W.; Perkhun, P.; Kammerer, J.; Alkarsifi, R.; Würfel, U.; Margeat, O.; Videlot-Ackermann, C.; Simon, J.-J.; Schröder, R. R.; Ackermann, J.; et al. Visualizing morphological principles for efficient photocurrent generation in organic non-fullerene acceptor blends. *Energy & Environmental Science* **2020**, *13* (4), 1259-1268, 10.1039/C9EE03535D.

(52) Dudenko, D.; Kiersnowski, A.; Shu, J.; Pisula, W.; Sebastiani, D.; Spiess, H. W.; Hansen, M. R. A Strategy for Revealing the Packing in Semicrystalline π-Conjugated Polymers: Crystal Structure of Bulk Poly-3-hexyl-thiophene (P3HT). *Angewandte Chemie International Edition* **2012**, *51* (44), 11068-11072. DOI: https://doi.org/10.1002/anie.201205075.

(53) Zhong, W.; Zhang, M.; Freychet, G.; Su, G. M.; Ying, L.; Huang, F.; Cao, Y.; Zhang, Y.; Wang, C.; Liu, F. Decoupling Complex Multi-Length-Scale Morphology in Non-Fullerene Photovoltaics with Nitrogen K-Edge Resonant Soft X-ray Scattering. *Advanced Materials* **2022**, *34* (6), 2107316, https://doi.org/10.1002/adma.202107316.

(54) Zhu, W.; Spencer, A. P.; Mukherjee, S.; Alzola, J. M.; Sangwan, V. K.; Amsterdam, S. H.; Swick, S. M.; Jones, L. O.; Heiber, M. C.; Herzing, A. A.; et al. Crystallography, Morphology, Electronic Structure, and Transport in Non-Fullerene/Non-Indacenodithienothiophene Polymer:Y6 Solar Cells. *Journal of the American Chemical Society* **2020**, *142* (34), 14532-14547. DOI: 10.1021/jacs.0c05560.

(55) Xiao, C.; Wang, X.; Zhong, T.; Zhou, R.; Zheng, X.; Liu, Y.; Hu, T.; Luo, Y.; Sun, F.; Xiao, B.; et al. Hybrid Cycloalkyl-Alkyl Chain-Based Symmetric/Asymmetric Acceptors with Optimized Crystal Packing and Interfacial Exciton Properties for Efficient Organic Solar Cells. *Advanced Science* **2023**, *10* (7), 2206580. DOI: https://doi.org/10.1002/advs.202206580.

(56) Suhai, S. Theory of exciton–photon interaction in polymers: Polariton spectra of polydiacetylenes. *The Journal of Chemical Physics* **1986**, *85* (1), 611-615. DOI: 10.1063/1.451586.

(57) Aasmundtveit, K. E.; Samuelsen, E. J.; Mammo, W.; Svensson, M.; Andersson, M. R.; Pettersson, L. A. A.; Inganäs, O. Structural Ordering in Phenyl-Substituted Polythiophenes. *Macromolecules* **2000**, *33* (15), 5481-5489. DOI: 10.1021/ma9911389.

(58) Mukamel, S. *Principles of Nonlinear Optical Spectroscopy*; Oxford University Press, 1995.
(59) Bednarz, M.; Lapin, J.; McGillicuddy, R.; Pelzer, K. M.; Engel, G. S.; Griffin, G. B. Modeling Ultrafast Exciton Migration within the Electron Donor Domains of Bulk Heterojunction Organic Photovoltaics. *The Journal of Physical Chemistry C* **2017**, *121* (10), 5467-5479. DOI: 10.1021/acs.jpcc.6b11332.
(60) Hinchliffe, A. *Molecular Modelling for Beginners*; Wiley, 2005.
(61) Nave, C. R. *Broadening of Spectral Lines*; 2017.
(62) Bernath, P. *Spectra of Atoms and Molecules*; Oxford University Press, 1995.
(63) Kroh, D.; Eller, F.; Schötz, K.; Wedler, S.; Perdigón-Toro, L.; Freychet, G.; Wei, Q.; Dörr, M.; Jones, D.; Zou, Y.; et al. Identifying the Signatures of Intermolecular Interactions in Blends of PM6 with Y6 and N4 Using Absorption Spectroscopy. *Advanced Functional Materials* **2022**, *32* (44), 2205711, https://doi.org/10.1002/adfm.202205711.
(64) Yu, C.; Gross, P.; Ramakrishna, V.; Rabitz, H.; Mease, K. Selective excitation of molecular eigenstates using state-dependent optical field design. *Chemical Physics Letters* **1996**, *252* (5), 447-456. DOI: https://doi.org/10.1016/0009-2614(96)00200-X.
(65) MacFarlane, R. M.; Shelby, R. M. Homogeneous line broadening of optical transitions of ions and molecules in glasses. *Journal of Luminescence* **1987**, *36* (4), 179-207. DOI: https://doi.org/10.1016/0022-2313(87)90194-3.
(66) Lee, T. H.; Park, S. Y.; Park, W.-W.; Du, X.; Son, J. H.; Li, N.; Kwon, O.-H.; Woo, H. Y.; Brabec, C. J.; Kim, J. Y. Efficient Exciton Diffusion in Organic Bilayer Heterojunctions with Nonfullerene Small Molecular Acceptors. *ACS Energy Letters* **2020**, *5* (5), 1628-1635. DOI: 10.1021/acsenergylett.0c00564.
(67) Zhang, M.; Zhu, L.; Hao, T.; Zhou, G.; Qiu, C.; Zhao, Z.; Hartmann, N.; Xiao, B.; Zou, Y.; Feng, W.; et al. High-Efficiency Organic Photovoltaics using Eutectic Acceptor Fibrils to Achieve Current Amplification. *Advanced Materials* **2021**, *33* (18), 2007177, https://doi.org/10.1002/adma.202007177.
(68) Stephens, P.J; Devlin, F..J; Chabalowski, C.F; Frisch, M.J.; J.Phys.Chem. 98 **1994,** 11623-11627

Section 6: Gaussian Checkpoint & Octave Simulation Files

Gaussian .gjf, .log, .chk; .fchk files are available for: the monomer optimized ground state geometry, the monomer transition dipole, and the transition dipoles for all three axial pairs at varied spacings.

Octave .m files were developed that build: the PDBD-T-2F Hamiltonian matrix implementing the line dipole subroutine, the 4th order time propagation of the density matrix, the basis transformation script to sample the excitons or initial populations, the visualization script to simulate the absorption spectrum, and the visualization script to display the exciton spatial probability through time and space.